POLITECNICO DI TORINO
Repository ISTITUZIONALE

An optimization based 3D-1D coupling strategy for tissue perfusion and chemical transport during tumor-induced angiogenesis

(Article begins on next page)
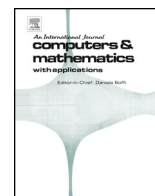
17 May 2024

An optimization based 3D-1D coupling strategy for tissue perfusion and chemical transport during tumor-induced angiogenesis

Stefano Berrone [1], Chiara Giverso [2], Denise Grappein [*],[1], Luigi Preziosi [2], Stefano Scialò [1]

Dipartimento di Scienze Matematiche, Politecnico di Torino, Corso Duca degli Abruzzi 24, 10129 Torino, Italy

ARTICLE INFO

ABSTRACT

The application of an optimization based 3D-1D coupling strategy is proposed, for the first time, for the simulation of fluid and chemical exchanges between a growing capillary network and the surrounding tissue, in the context of tumor-induced angiogenesis. A well posed mathematical model is worked out, based on the coupling between a three-dimensional and a one-dimensional equation (3D-1D coupled problem). The problems are then solved in a PDE-constrained optimization framework, under which no mesh conformity is required. This makes the method particularly suitable for this kind of application, since no remeshing is required as the capillary network grows. In order to handle both the evolution of the quantities of interest and the changes in the geometry, a discrete-hybrid strategy is adopted, combining a continuous modeling of the tissue and of the chemicals with a discrete tip-tracking model to account for the vascular network growth. The tip-tracking strategy, together with some proper rules for branching and anastomosis, is able to provide a realistic representation of the capillary network.

1. Introduction

Angiogenesis is the crucial process that leads to the formation of new blood vessels from an existing vasculature, with the aims of providing the correct amount of nutrients and oxygen to the tissue and of warranting metabolic waste removal from it [1]. This process occurs in many different conditions, either physiologically (e.g., embryogenesis, wound-healing, and female cycle) [2,3] or pathologically (e.g., rheumatoid and inflammatory disease, duodenal ulcers, abnormal vascularization in the eye, and the initiation and progression of cancers) [4–8]. In all cases, angiogenesis entails a well-organized sequence of events, comprising the rearrangement, migration, and proliferation of endothelial cells (ECs) forming the capillary wall. These processes should coordinate with the establishment of blood flow inside the new capillaries in order to reach a properly functional vessel network [9]. The whole process is orchestrated by biochemical stimuli, released both by neighboring cells and by the ECs themselves, and by the mechanical interaction between the ECs and the surrounding environment (refer to [10–13] for an extensive review of the key chemical and mechanical cues in angiogenesis).

In this paper, we specifically focus on tumor-induced angiogenesis, occurring when an avascular tumor reaches a critical diameter of approximately 1-2 mm, above which nutrients and oxygen diffusion from the existing vasculature are no longer sufficient to sustain cancer progression and cells inside the tumor experience hypoxia [9,14]. The hypoxic condition triggers the secretion by tumor cells of a number of chemicals, collectively called *tumor angiogenic factors* (TAFs) [1,9]. These substances diffuse through the nearby tissue and, when they reach the vasculature, they activate ECs by binding to the transmembrane cell receptors and activating specific molecular pathways. This initiates the first step of angiogenesis, in which ECs change shape and adhesion properties, leading to a weakening of the junctions within the endothelial layer and a subsequent increase in the permeability of the blood vessel [15]. In the next phase, ECs produce proteolytic enzymes, which degrade the basal lamina of the vessel and the surrounding extracellular matrix [16], enabling the formation of the first protrusion (*sprout*) and the subsequent cell migration towards the source of the TAFs (*chemotaxis*) [17,18]. At this stage, it is possible to distinguish between *tip* cells, i.e., the specialized cells at the extremity of newly

---

* Corresponding author.
  E-mail addresses: stefano.berrone@polito.it (S. Berrone), chiara.giverso@polito.it (C. Giverso), denise.grappein@polito.it (D. Grappein), luigi.preziosi@polito.it (L. Preziosi), stefano.scialo@polito.it (S. Scialò).
[1] Member of INdAM research group GNCS.
[2] Member of INdAM research group GNFM.

formed capillaries that guide vessel outgrowth through chemotactic motion, and *stalk* cells, which are highly proliferative cells that follow the tip cell motion, establishing tight junctions to ensure the stability of the new sprout and the formation of the nascent capillary [19]. During the development of the network, tip-sprouts may undergo *branching* or they can merge when two capillaries encounter each other (*anastomosis*) [17,20]. As the sprout approaches the tumor, the branches noticeably increase in number [21] and the whole process culminates with the penetration of the new capillaries inside the tumor. Once the tumor becomes vascularized, the cancer cells gain access to an almost unlimited supply of nutrients and oxygen and they can eventually enter inside the vasculature and form metastasis also in distant sites [11].

Tumor-induced angiogenesis has been extensively studied through *in vitro* and *in vivo* biological experiments [22–25], that pointed out the main biomechanical factors and pathways involved in both physiological and pathological vascular progression. However, many aspects are still under investigation and a comprehensive biological set-up able to study the process as a whole, considering the different spatio-temporal scales and all the components involved in this complex mechanism is yet to be developed. In this regard, *in silico* models may be an efficient way to study and replicate selected features of the experimental system and forecast the evolution of the entire process in biologically relevant conditions. Therefore, in the last decades, different mathematical models have been proposed, with different approaches, from continuous [26–33] to discrete/hybrid [34–38] models, with either deterministic or stochastic rules for cell branching (see [39–41] for a review on mathematical models on angiogenesis). Continuous models [26,28,29,42], typically encapsulates systems of coupled nonlinear partial differential equations (PDEs) describing the migration of ECs from the parent vessel towards the solid tumor in response to the TAFs and other chemicals dispersed in the ECM or eventually released by the ECs themselves. Despite the ability of such PDE models to capture important angiogenic features at the macroscopic scale (i.e., average ECs and sprout density, average vessel growth and network expansion rates), they are not able to explicitly represent the geometry of the developing capillary network. Even in those cases in which the boundary between the capillary network and the surrounding tissue is tracked through a diffuse interface approach [32,41], the proposed models are not suitable to evaluate the inner blood flow. At the same time, in those continuous models in which the morphology of nascent vessels is captured through a sharp interface, whose evolution is controlled both by chemical and mechanical cues [33], the vascularization of the network is not described, since it would require the definition of the complex fluid-structure interaction in an evolving 3D network. Conversely, the description of the vessel network morphology has been widely reproduced with discrete models operating at the scale of single ECs [20,43], coupled with a continuous representation for the chemicals [34,42,44,45,37,46,38]. Although hybrid models have the advantage of describing the motion of individual ECs for simulating a realistic capillary network, the number of vessels that can be considered is limited by the computational costs of the discrete representation of each EC. Furthermore, the simulation of the blood flow inside the expanding geometry is generally disregarded. Indeed, despite its renowned importance in tumor growth and drug transport, the study of blood flow through the new vessel network and the mechanisms of fluid transport inside the surrounding tissue have only recently gained attention in mathematical modeling.

Starting from the preliminary works of Baxter and Jain presenting a macroscopic model for fluid and macromolecules transport inside a tumor with a distributed vascular source [47,48] and a microscopic model describing flow transport around a single vessel [49], some mathematical models to describe the blood flow in non-evolving vascular networks have been proposed [50,51]. Recently some attempts to couple discrete models of angiogenesis, with continuous models of blood flow have been done. Specifically, in [52], the flow into each node of a network of vessels, evolving accordingly to the discrete angiogenesis model proposed in [53], is expressed in terms of nodal pressures

and flow resistances of the segment, in order to satisfy the conservation of mass. A similar approach to determine blood flow in the vessel was used in [36,54–56], with different discrete models to reproduce the spatial and temporal evolution of the network. In these works, the simulation of flow was carried out a posteriori, either after generation of an hexagonal hollow vessel network constructed ad-hoc [36] or after an initial cell migration model that reproduce the vessel network [54–56]. Notably, Rieger et al. developed a 2D and 3D cellular automata model [57–59] that considered angiogenesis, vessel co-option and vessel collapse in a time-dependent model of blood flow and tumor growth. However, in all these models, nascent vessels need to be conformal to the mesh, leading to unnatural geometries of the network and blood flow inside it. Furthermore when cellular automata are used, the number of cells that can be simulated and therefore the extent of the vascular network that can be reproduced are limited in size. More complex models for vessel generation and blood flow simulation inside both the evolving capillary network and the surrounding tissue can be found in [60,61]. In particular, in [60] an algorithmic approach to generate realistic microvascular networks starting from larger vessels and a numerical method to solve the 3D-1D coupled model for blood flow and oxygen transport are presented. In that work, Murray's law is used to determine the radii of the vessels and the bifurcation angles, without any influence of the chemical involved in the angiogenesis process. Therefore this model can be more suitably applied to obtain surrogate vessel networks than to study tumor-induced angiogenesis. The resulting problem is solved with a two-point flux approximation scheme, with singular sources described as Dirac deltas for the 3D-1D coupling. On the other hand, the work of [61] focuses on modeling and simulating the growth of a tumor sustained by an evolving vessel networks. The 3D model for the tissue is based on continuous balance laws for a mixture composed by the tumor tissue, the extracellular matrix and the chemicals (namely the tumor angiogenic factors and the matrix-degrading enzymes). All the phases in the mixture are constrained to move with the same velocity and a Cahn-Hilliard type phase-field model is used to separate them. Angiogenesis is orchestrated both by some deterministic rules related to the concentration of the tumor angiogenesis factors and by the presence of stochastic terms. The equation system is solved using a combination of finite volume and finite element schemes and an iterative procedure is used to couple the 3D and 1D problems. The numerical results [61], however, refer to a network with a limited number of vessels.

Therefore in this work, neglecting the growth of the tumor mass, we focus on the angiogenesis process in order to propose an efficient numerical technique to solve the fluid flow and chemical transport problems both inside the tissue and inside the vessels. Specifically, we propose a hybrid model, coupling a continuous representation of the tissue and of the chemical dispersed inside it with a discrete tip-tracking model that describes the motion of tip cells and the subsequent formation of vessels. In principle this task would require the definition of a three dimensional domain, representing the healthy tissue, with tubular evolving structures immersed inside it, to represent the vessels. Then, all the equations of the model should be defined in both domains, with proper conditions at the interface between the vessel and the surrounding tissue. The presence of domains with embedded tubular inclusions with radius much smaller than the length and than the size of the domain itself is challenging from a simulation standpoint. The generation of the computational mesh in the interior of the inclusions, indeed, constraints the mesh-size in the neighborhood, thus resulting in a linear system with a very large number of unknowns. Further, for complex networks of inclusions, the mesh generation process may be infeasible, due to the large number of geometrical constraints. All these complexities are further aggravated if time-dependent simulations are to be performed and when branching and anastomosis occur.

The reduction of the inclusions to one dimensional objects can be performed, in these situations, to mitigate the computational cost and to allow the treatment of arbitrarily complex configurations. The 3D
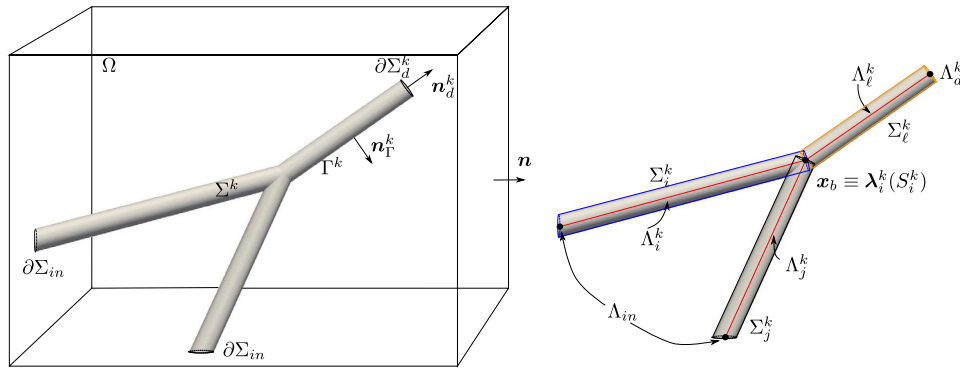
Fig. 1. Nomenclature for capillary network representation at a bifurcation point.

inclusions are collapsed on their centrelines, and simultaneously the external domain is extended to fill the voids. The resulting problem is composed of a three dimensional bulk domain with an embedded network of one dimensional domains, and a coupling of the solutions of such 3D-1D problems is required.

The mathematical formulation of 3D-1D coupled problems requires particular care, as there is no bounded trace operator on 1D manifolds for functions in H^1-spaces on 3D domains. In [62,63] 3D problems with singular source terms on 1D segments are investigated, posing the basis for the analysis of 3D-1D coupled problems. Some authors suggest a regularization of the singular terms, such as in [64–66], or splitting techniques, which treat in a separate manner the regular and irregular part of the solution [67,68]. Coupled 3D-1D problems are treated by [69] through the introduction of suitable averaging operators, and by [70] through the use of Lagrange multipliers in a domain decomposition setting. Here the method proposed by [71,72] is adopted, in which a well posed problem is derived in suitable function spaces, defined on the basis of some assumptions on the regularity of the solution, and the problem is solved by means of an optimization based domain decomposition method. According to this approach, the 3D problem and the 1D problem are independently written, introducing additional variables at the interfaces, and a cost functional, expressing the error in fulfilling interface conditions is minimized to recover a global solution. The advantages of this approach lie in the possibility of building independent meshes on the various domains and in the direct computation of interface variables, that are of particular interest for the applications.

In detail, the paper is organized as follows. In Section 2 we introduce the notation and the main modeling assumptions. The governing equations of the angiogenesis hybrid model, described as a 3D-1D coupled problem, are presented in Section 3, while in Section 4 the optimization based domain decomposition for 3D-1D coupling is proposed and analyzed. Section 5 is devoted to the discussion of the details concerning the numerical discretization of the model equations, while in Section 6 some numerical experiments are presented. Finally, in Section 7 we summarize the main features of the work and present possible directions for further research.

2. Notation and model assumptions

Let us consider the time interval $[0, T]$ and a partition defined as

$$0 = t_0 < t_1 < ... < t_k < ... < t_K = T,$$

with $\mathcal{I}_k = (t_{k-1}, t_k]$ and $\Delta \mathcal{I}_k = t_k - t_{k-1}$. Let $\Sigma(t_k) = \Sigma^k \subset \Omega \subset \mathbb{R}^3$ denote the capillary network at time t_k. For the sake of simplicity we consider the case $\Sigma^0 \subseteq \Sigma^1 \subseteq ... \subseteq \Sigma^k$, i.e. we allow for the growth of the vascular network by so-called *sprouting angiogenesis*, but not for its regression. More precisely, in a continuous-discrete hybrid framework, Σ^k denotes the fixed capillary network which is considered as the quantities of interest vary during the time-interval $\mathcal{I}_k$. We assume that the network Σ^k

is composed by thin tubular vessels of constant radius R, as shown in Fig. 1, the generalization to a radius varying along the network being however straightforward. The surrounding interstitial volume for $t \in \mathcal{I}_k$ is defined as $\mathcal{D}^k = \Omega \setminus \overline{\Sigma^k}$. The boundary of Ω is denoted by $\partial\Omega$ whereas $\partial\Sigma^k$ is the boundary of Σ^k. Such boundary is split into four parts, i.e.

$$\partial\Sigma^k = \Gamma^k \cup \left(\partial\Sigma_{in}^k \cup \partial\Sigma_{out}^k \cup \partial\Sigma_d^k \right),$$

with Γ^k denoting the lateral surface of Σ^k, and $\partial\Sigma_{in}^k \subset \partial\Omega$ and $\partial\Sigma_{out}^k \subset \partial\Omega$ being the union, respectively, of the inlet and outlet cross-sections of Σ^k, the nomenclature referring to blood velocity. Finally, the set $\partial\Sigma_d^k$ collects the extremal cross sections of Σ^k lying in the interior of Ω and thus having an empty intersection with $\partial\Omega$. We will assume that the extremal cross sections of Σ^k are either completely lying on $\partial\Omega$, or inside Ω, for all $k = 0, ..., K$. For clarity of exposition, we also suppose the set of the inflow and outflow sections to be fixed in time, i.e. we exclude the possibility for any growing vessel to reach the boundary of the domain. For this reason the sets $\partial\Sigma_{in}$ and $\partial\Sigma_{out}$ will actually not depend on time, so that the superscript k is dropped. On the other hand, $\partial\Sigma_d^k$ is allowed to change in time. In practice, Ω will bound the entire vessel network generated by angiogenesis and encompass the region in which chemical diffusion and transport take place. In Fig. 1, we have reported a simplified cartoon of a single bifurcation just to provide clear labels for the vessel geometry. Vectors $\tilde{n}_{out}$ and $\tilde{n}_d^k$ are used to denote the unit normal vectors to $\partial\Sigma_{out}$ and $\partial\Sigma_d^k$ respectively, both outward pointing from Σ^k. We define the boundary of $\mathcal{D}^k$ as

$$\partial\mathcal{D} = \partial\Omega \setminus (\partial\Sigma_{in} \cup \partial\Sigma_{out}),$$

where the superscript k is dropped since $\partial\Sigma_{in}$ and $\partial\Sigma_{out}$ do not change in time. We denote by n the unit normal vector to $\partial\mathcal{D}$ outward pointing from $\mathcal{D}^k$.

We assume that the radius R is much smaller than the inclusion length and than the characteristic size of Ω, and thus that the original 3D-3D equi-dimensional problems can be approximated by 3D-1D problems. First, in each time interval $\mathcal{I}_k$, the original network Σ^k is covered by a set of thin straight cylindrical vessels Σ_i^k, eventually cut by domain borders. We denote the centerline of each cylindrical vessel segment by $\Lambda_i^k = \{\lambda_i^k(s), \ s \in (0, S_i^k)\}$, for $i \in Y^k$, where Y^k is the set of vessel segment indices in $\mathcal{I}_k$. We also call Γ_i^k the lateral surface of each vessel. Vessel centrelines are possibly connected at their endpoints, and we denote by $\{x_b\}_{b \in B^k}$ the set of points at which vessel centrelines join or bifurcate as a consequence of branching or anastomosis events. The subset $Y_b^k \subset Y^k$ of centreline indexes is introduced, such that segments Λ_j^k, $j \in Y_b^k$ are connected in x_b, and we call $S_{i,b}$ the curvilinear abscissa such that $\lambda_i^k(S_{i,b}) = x_b$, $i \in Y_b^k$ (clearly $S_{i,b}$ is either 0 or S_i^k). The domain Σ^k is thus replaced, in the derivation of the 3D-1D problems, by $\bigcup_{i \in Y^k} \Sigma_i^k$, while $\Lambda^k = \bigcup_{i \in Y^k} \Lambda_i^k \cup \{x_b\}_{b \in B^k}$, with Λ_{in}, Λ_{out} and Λ_d^k denoting respectively the union of the centers of the sections in $\partial\Sigma_{in}$, $\partial\Sigma_{out}$ and $\partial\Sigma_d^k$. We remark that, in general, according to the above definition,
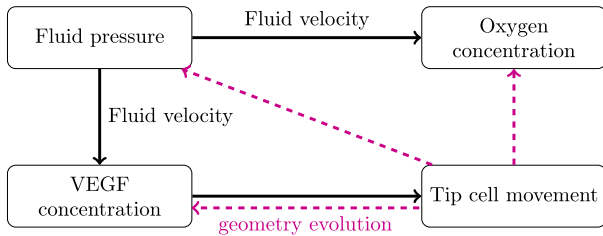
Fig. 2. Mutual dependence of the considered problems/quantities.

the union of the Σ_i^k might be different from Σ^k, but, as R is small such difference can be considered negligible.

3. Models and methods

The process of oxygen delivery by blood flow during angiogenesis is here described by means of three partial differential equation problems and an ordinary differential equation. In particular, we consider a PDE problem for fluid pressure, one for oxygen concentration, and another for VEGF concentration. The growth of the capillary network is described by an ODE for the evolution of the position of vessel free ends, with given rules for preferential growth paths, branching and anastomosis. The starting point is an equilibrium configuration at time $t = 0$ for pressure, oxygen concentration, and VEGF concentration in the domain, given the initial vessel configuration Σ_0. Then the vessel network can change, over a given time interval, with the displacement of vessel tip cells depending on the initial VEGF concentration. The new computed geometry, Σ_1, breaks the equilibrium configuration, triggering the evolution of pressure, VEGF and oxygen concentration, over the same time interval. First, the new pressure distribution is calculated and post processed to determine fluid velocity both in the vessels and in the interstitial tissue. Such velocity is then used to compute the new distribution of VEGF and oxygen concentration. When calculating the evolution of such quantities, the geometry of the vessel is kept fixed at Σ_1. The whole process is then repeated over the next time interval, starting again from the growth of the network, according to the new concentration of VEGF. A diagram of the process modeling is shown in Fig. 2. In the following the different problems are analyzed in details, while a summary of the equations is provided in Section 3.5.

3.1. The pressure problem

The first PDE problem describes the distribution of fluid pressure in the considered domain. This problem is first formulated as a coupled problem between a 3D tissue and a 3D domain given by the union of the vessels. To ease the meshing process and to reduce the computational cost of simulations, since the radius of the vessels is small compared to the size of the whole domain Ω, the 3D-3D equi-dimensional problem is re-formulated as a 3D-1D coupled problem, assuming that, inside the vessels, the variation of pressure along the cross section is negligible. The pressure problem is solved in a quasi-stationary framework, i.e. an equilibrium problem is solved each time the geometry is updated. For details about the solving strategy we refer to Sections 4-5, that refer to the oxygen concentration problem but can be easily generalized to the pressure case.

Let us denote by $p(\boldsymbol{x}, t)$ and $\tilde{p}(\boldsymbol{x}, t)$ respectively the interstitial fluid pressure in the tissue $\mathcal{D}^k$ and the blood pressure in the capillary network Σ^k, with $t \in \mathcal{I}_k = (t_{k-1}, t_k]$. Assuming that the tissue can be suitably represented by a saturated porous medium [73], with the cells and the extracellular matrix representing the solid skeleton, the Darcy's law can be used to model the interstitial flow. The solid skeleton is assumed to be rigid and the growth of cells in the tissue surrounding the capillary and the degradation/deposition of the ECM are neglected. Therefore the cell volume fraction of the interstitial fluid and the solid phase can be assumed constant. Inside the capillaries, the motion of

the blood, described as an incompressible viscous fluid can be appropriately described by the Poiseuille's law for laminar stationary flow [47,50]. Therefore, the following 3D-3D quasi-stationary coupled problem completely describes the motion of the fluid inside the capillary and the interstitium $\forall t \in \mathcal{I}_k$:

$$-\nabla \cdot \left(\frac{\kappa}{\mu} \nabla p(\boldsymbol{x}, t) \right) + \beta_p^{LS} \frac{S}{V}(p(\boldsymbol{x}, t) - p_{LS}) = 0 \qquad \boldsymbol{x} \in \mathcal{D}^k \tag{1}$$

$$\frac{\kappa}{\mu} \nabla p(\boldsymbol{x}, t) \cdot \boldsymbol{n}_\Gamma^k(\boldsymbol{x}) = \beta_p(\tilde{p}(\boldsymbol{x}, t) - p(\boldsymbol{x}, t) - \Delta p_{onc}) \qquad \boldsymbol{x} \in \Gamma^k \tag{2}$$

$$\frac{\kappa}{\mu} \nabla p(\boldsymbol{x}, t) \cdot \boldsymbol{n}(\boldsymbol{x}) = \beta_p^{ext}(p_{ext} - p(\boldsymbol{x}, t)) \qquad \boldsymbol{x} \in \partial D \tag{3}$$

$$\nabla p(\boldsymbol{x}, t) \cdot \boldsymbol{n}_d^k(\boldsymbol{x}) = 0 \qquad \boldsymbol{x} \in \partial \Sigma_d^k \tag{4}$$

$$-\nabla \cdot \left(\frac{R^2}{8\mu} \nabla \tilde{p}(\boldsymbol{x}, t) \right) = 0 \qquad \boldsymbol{x} \in \Sigma^k \tag{5}$$

$$\frac{R^2}{8\mu} \nabla \tilde{p}(\boldsymbol{x}, t) \cdot \tilde{\boldsymbol{n}}_\Gamma^k(\boldsymbol{x}) = \beta_p(p(\boldsymbol{x}, t) - \tilde{p}(\boldsymbol{x}, t) + \Delta p_{onc}) \qquad \boldsymbol{x} \in \Gamma^k \tag{6}$$

$$\tilde{p}(\boldsymbol{x}, t) = \tilde{p}_{in} \qquad \boldsymbol{x} \in \partial \Sigma_{in} \tag{7}$$

$$\tilde{p}(\boldsymbol{x}, t) = \tilde{p}_{out} \qquad \boldsymbol{x} \in \partial \Sigma_{out} \tag{8}$$

$$\nabla \tilde{p}(\boldsymbol{x}, t) \cdot \tilde{\boldsymbol{n}}_d^k(\boldsymbol{x}) = 0 \qquad \boldsymbol{x} \in \partial \Sigma_d^k. \tag{9}$$

Parameters κ and μ are positive scalars, denoting respectively the hydraulic permeability of the tissue and blood viscosity. Also β_p and β_p^{ext} are positive scalars, representing respectively the permeability of the capillary wall Γ^k and the conductivity of the external boundary, while p_{ext} is the basal pressure. In numerical simulations we will consider $\tilde{p}_{out} = p_{ext}$. Vector $\boldsymbol{n}_\Gamma^k = -\tilde{\boldsymbol{n}}_\Gamma^k$ is the unit normal vector to Γ^k outward pointing from $\mathcal{D}^k$, while $\boldsymbol{n}_d^k = -\tilde{\boldsymbol{n}}_d^k$.

Equations (1) and (5) are coupled through (2) and (6), which impose flux conservation across the surface Γ^k. The flux is defined through the Starling equation, assuming it is proportional to the pressure jump. The term Δp_{onc} accounts for the contribution of oncotic pressure, whose gradient is determined by the difference in concentration of the chemicals on the two sides of the vessel wall. The most significant contribution to the oncotic pressure gradient is given by proteins, in particular by albumin, whose concentration is considered constant. For this reason we handle the oncotic pressure as a known correction term $\Delta p_{onc} = \xi(\tilde{p}_{onc} - p_{onc})$, with p_{onc} and $\tilde{p}_{onc}$ denoting the oncotic pressure of albumin inside $\mathcal{D}^k$ and Σ^k respectively ($\forall k$) and ξ being the departure of the membrane from perfect permeability (see [51] for further details). Finally the term $\beta_p^{LS} \frac{S}{V}(p(\boldsymbol{x}, t) - p_{LS})$ accounts for the absorption of the fluid in excess by the lymphatic system. This contribution is treated as a distributed sink term, with β_p^{LS} denoting the permeability of the lymphatic wall, $\frac{S}{V}$ the surface area of lymphatic vessels per unit of tissue volume and $p_{LS} = p_{ext}$ the pressure inside the lymphatic system. Once the pressure distribution is computed inside $\mathcal{D}^k$ and Σ^k the fluid velocity can be defined as

$$\boldsymbol{v}(\boldsymbol{x}, t) = -\frac{\kappa}{\mu} \nabla p(\boldsymbol{x}, t) \quad \boldsymbol{x} \in \mathcal{D}^k, \ t \in \mathcal{I}_k \tag{10}$$

$$\tilde{\boldsymbol{v}}(\boldsymbol{x}, t) = -\frac{R^2}{8\mu} \nabla \tilde{p}(\boldsymbol{x}, t) \quad \boldsymbol{x} \in \Sigma^k, \ t \in \mathcal{I}_k. \tag{11}$$

In order to reduce the problem to a 3D-1D coupled problem let us assume that, inside the vessels, the pressure variations along the radial direction are negligible and let us hence introduce, $\forall i \in Y^k$, the one-dimensional quantity $\hat{p}_i(s, t)$ such that, in cylindrical coordinates, for $s \in (0, S_i^k)$ and $t \in \mathcal{I}_k$

$$\tilde{p}_{|\Sigma_i^k}(r, \theta, s, t) = \hat{p}_i(s, t), \qquad \forall r \in [0, R], \ \forall \theta \in [0, 2\pi). \tag{12}$$

Similarly we introduce the one-dimensional quantity $\breve{p}_i(s, t)$ such that

$$p_{|\Gamma_i^k}(R, \theta, s, t) = \breve{p}_i(s, t), \qquad \forall \theta \in [0, 2\pi), \tag{13}$$

i.e. we are neglecting the variations of $p(\boldsymbol{x}, t)$ along the cross section perimeter.
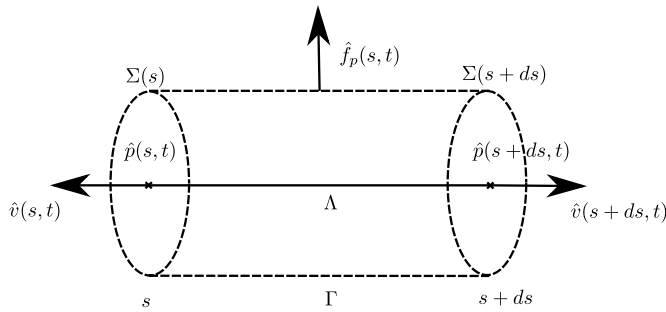
Fig. 3. Sketch of the 1D reduced problem with related quantities.

Thus, defining for $s \in (0, S_i^k)$, $t \in \mathcal{I}_k$:

$$\hat{f}_p^i(s,t) = 2\pi R \beta_p (\hat{p}_i(s,t) - \check{p}_i(s,t) - \Delta p_{onc}), \tag{14}$$

$$\hat{v}_i(s,t) = -\frac{R^2}{8\mu} \frac{\partial \hat{p}_i(s,t)}{\partial s}, \quad Q_i(s,t) = |\Sigma_i(s)| \hat{v}_i(s,t),$$

and given the assumptions on the geometry, the conservation law on vessel centerline reads (see Fig. 3):

$$Q_i(s+\mathrm{d}s, t) = Q_i(s,t) - \hat{f}_p^i(s,t)\,\mathrm{d}s.$$

Therefore equations (1)-(2) and (5)-(6) can be rewritten as a 3D-1D coupled system, i.e. for $t \in \mathcal{I}_k$:

$$-\nabla \cdot \left(\frac{\kappa}{\mu} \nabla p(\boldsymbol{x},t) \right) + \beta_p^{LS} \frac{S}{V}(p(\boldsymbol{x},t) - p_{LS}) = \sum_{i \in Y^k} \hat{f}_p^i \delta_{\Lambda_i^k} \qquad \boldsymbol{x} \in \mathcal{D}^k \quad (15)$$

$$-\frac{\partial}{\partial s}\left(\frac{\pi R^4}{8\mu} \frac{\partial \hat{p}_i(s,t)}{\partial s} \right) = -\hat{f}_p^i(s,t) \qquad \forall i \in Y^k,\ s \in (0, S_i^k) \quad (16)$$

$$\sum_{j \in Y_b} \frac{\partial \hat{p}_j}{\partial s}(S_{j,b}, t) = 0 \qquad \forall b \in B^k \quad (17)$$

$$\hat{p}_i(S_{i,b}, t) = \hat{p}_j(S_{j,b}, t) \qquad \forall i \neq j \in Y_b,\ \forall b \in B^k, \quad (18)$$

where the last two equations express respectively flux balance and pressure continuity at bifurcation points. We observe that the flow through the lateral surface of each vessel, $\hat{f}_p^i$ behaves as a distributed source term in the 1D reduced problem (16), balanced by the corresponding concentrated source terms in the 3D problem (15). More details on geometrical model reduction, also considering more general vessel geometries, can be found in [69].

3.2. The oxygen concentration problem

Similarly to the pressure case, we start from an equidimensional 3D-3D coupled problem, concerning the transport and diffusion of oxygen in the tissue and inside the vessel network. The velocity field for the transport term is computed according to the gradient of fluid pressure, previously obtained. In this case the equations are parabolic, i.e. although the geometry is fixed $\forall t \in \mathcal{I}_k$, we consider the continuous variation of oxygen distribution in the given time-interval. Exploiting the same considerations that were done for pressure, we reduce the problem to a 3D-1D coupled problem. The reformulation as an optimization based problem and its discretization are given in Sections 4-5.

Denoting by $c(\boldsymbol{x},t)$ and $\tilde{c}(\boldsymbol{x},t)$ the concentration of oxygen respectively in $\mathcal{D}^k$ and in the capillary network Σ^k, we can write, for $t \in \mathcal{I}_k$ the following 3D-3D reaction-diffusion-convection coupled problem:

$$\frac{\partial c(\boldsymbol{x},t)}{\partial t} = \nabla \cdot \left(D_c \nabla c(\boldsymbol{x},t) - \boldsymbol{v}(\boldsymbol{x},t) \cdot \nabla c(\boldsymbol{x},t) - m_c(c(\boldsymbol{x},t)) \right) \quad \boldsymbol{x} \in \mathcal{D}^k \quad (19)$$

$$D_c \nabla c(\boldsymbol{x},t) \cdot \boldsymbol{n}_\Gamma^k(\boldsymbol{x}) = \beta_c(\tilde{c}(\boldsymbol{x},t) - c(\boldsymbol{x},t)) \qquad \boldsymbol{x} \in \Gamma^k \quad (20)$$

$$D_c \nabla c(\boldsymbol{x},t) \cdot \boldsymbol{n}(\boldsymbol{x}) = \beta_c^{ext}(c_{ext} - c(\boldsymbol{x},t)) \qquad \boldsymbol{x} \in \partial D \quad (21)$$

$$\nabla c(\boldsymbol{x},t) \cdot \boldsymbol{n}_d^k(\boldsymbol{x}) = 0 \qquad \boldsymbol{x} \in \partial \Sigma_d^k \quad (22)$$

$$\frac{\partial \tilde{c}(\boldsymbol{x},t)}{\partial t} = \nabla \cdot (\tilde{D}_c \nabla \tilde{c}(\boldsymbol{x},t)) - \tilde{\boldsymbol{v}}(\boldsymbol{x},t) \cdot \nabla \tilde{c}(\boldsymbol{x},t) \qquad \boldsymbol{x} \in \Sigma^k \quad (23)$$

$$\tilde{c}(\boldsymbol{x}, t_{k-1}) = 0 \qquad \boldsymbol{x} \in \Sigma^k \setminus \Sigma^{k-1} \quad (24)$$

$$\tilde{D}_c \nabla \tilde{c}(\boldsymbol{x},t) \cdot \tilde{\boldsymbol{n}}_\Gamma^k(\boldsymbol{x}) = \beta_c(c(\boldsymbol{x},t) - \tilde{c}(\boldsymbol{x},t)) \qquad \boldsymbol{x} \in \Gamma^k \quad (25)$$

$$\tilde{c}(\boldsymbol{x},t) = c_{in} \qquad \boldsymbol{x} \in \partial \Sigma_{in} \quad (26)$$

$$\tilde{D}_c \nabla \tilde{c}(\boldsymbol{x},t) \cdot \tilde{\boldsymbol{n}}_{out}(\boldsymbol{x}) = 0 \qquad \boldsymbol{x} \in \partial \Sigma_{out} \quad (27)$$

$$\nabla \tilde{c}(\boldsymbol{x},t) \cdot \tilde{\boldsymbol{n}}_d^k(\boldsymbol{x},t) = 0 \qquad \boldsymbol{x} \in \partial \Sigma_d^k. \quad (28)$$

For $k = 0$ we define the initial conditions

$$c(\boldsymbol{x}, t_0) = c_0(\boldsymbol{x}) \qquad \boldsymbol{x} \in \mathcal{D}^0$$

$$\tilde{c}(\boldsymbol{x}, t_0) = \tilde{c}_0(\boldsymbol{x}) \qquad \boldsymbol{x} \in \Sigma^0$$

while for $k > 0$ the concentrations at time t_{k-1} are available from the final concentrations computed in $\mathcal{I}_{k-1}$ and only the amount of oxygen in the newborn capillaries has to be initialized, as in equation (24). Parameters D_c and $\tilde{D}_c$ are positive scalars denoting the diffusivity respectively in $\mathcal{D}^k$ and Σ^k. Also β_c and β_c^{ext} are positive scalars, which denote the permeability to oxygen respectively of the blood vessel wall and of the boundary of $\mathcal{D}^k$. Finally, function $m_c(c(\boldsymbol{x},t))$ accounts for the oxygen metabolization by cells. In particular we choose $m_c(c(\boldsymbol{x},t)) = M_c c(\boldsymbol{x},t)$, with M_c positive scalar.

As for the pressure case, let us introduce $\forall i \in Y_k$ the one-dimensional quantities $\hat{c}_i(s,t)$ and $\check{c}_i(s,t)$, $s \in (0, S_i^k)$, and let us assume that for $s \in (0, S_i^k)$ and $t \in \mathcal{I}_k$

$$\tilde{c}_{|\Sigma_i^k}(r, \theta, s, t) = \hat{c}_i(s,t), \qquad \forall r \in [0, R],\ \forall \theta \in [0, 2\pi] \quad (29)$$

$$c_{|\Gamma_i^k}(R, \theta, s, t) = \check{c}_i(s,t), \qquad \forall \theta \in [0, 2\pi]. \quad (30)$$

Defining the quantity

$$\hat{f}_c^i(s,t) = 2\pi R \beta_c(\hat{c}_i(s,t) - \check{c}_i(s,t)), \qquad s \in (0, S_i^k),\ t \in \mathcal{I}_k \quad (31)$$

equations (19)-(20) and (23)-(25) can now be rewritten as the 3D-1D coupled system, for $t \in \mathcal{I}_k$:

$$\frac{\partial c(\boldsymbol{x},t)}{\partial t} - \nabla \cdot \left(D_c \nabla c(\boldsymbol{x},t) \right) + \boldsymbol{v}(\boldsymbol{x},t) \cdot \nabla c(\boldsymbol{x},t) + m_c(c(\boldsymbol{x},t)) = \sum_{i \in Y^k} \hat{f}_c^i \delta_{\Lambda_i^k} \quad (32)$$

$$\boldsymbol{x} \in \mathcal{D}^k$$

$$\pi R^2 \frac{\partial \hat{c}_i(s,t)}{\partial t} - \frac{\partial}{\partial s_i}\left(\pi R^2 \tilde{D}_c \frac{\partial \hat{c}_i(s,t)}{ds} \right) + \pi R^2 \hat{v}_i(s,t) \frac{\partial \hat{c}_i(s,t)}{\partial s_i} = -\hat{f}_c^i(s,t) \quad (33)$$

$$\forall i \in Y^k,\ s \in (0, S_i^k)$$

$$\sum_{j \in Y_b} \frac{\partial \hat{c}_j}{\partial s}(S_{j,b}, t) = 0 \qquad \forall b \in B^k \quad (34)$$
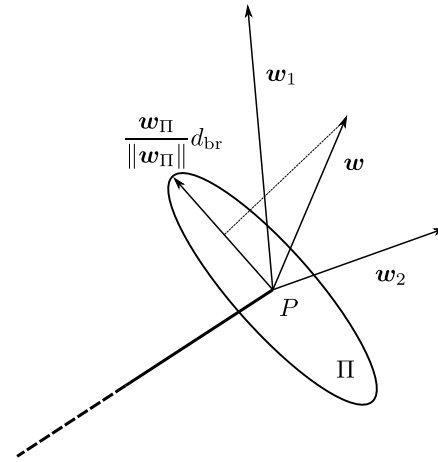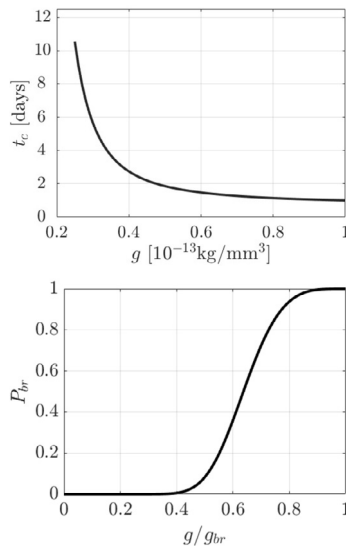
$$\hat{c}_i(S_{i,b}, t) = \hat{c}_j(S_{j,b}, t) \qquad \forall i \neq j \in Y_b,\ \forall b \in B^k. \quad (35)$$

3.3. The chemotactic growth factor problem

The third considered PDE models the distribution of a chemotactic growth factor in the 3D tissue. The absorption of the chemotactic agent by the capillary network is modeled as a singular sink term located at vessel centrelines, while no equation is solved inside the vessel network. Even in this case a time-dependent advection-diffusion-reaction equation is considered.

Let us denote by $C \subset \mathbb{R}^3$ the portion of space occupied by the tumor. We suppose that $\partial \Omega \cap \partial C \neq \emptyset$ but $C \nsubseteq \Omega$, i.e. our computational domain does not account for the tumor region, but a portion of its boundary is chosen as an interface with the tumor itself. Let us then denote by $g(\boldsymbol{x},t)$ the concentration of a vascular endothelial growth factor (VEGF) and let us describe its evolution for $t \in \mathcal{I}_k$ by the following set of equations

$$\frac{\partial g(\boldsymbol{x},t)}{\partial t} = \nabla \cdot \left(D_g \nabla g(\boldsymbol{x},t) - \boldsymbol{v}(\boldsymbol{x},t) \cdot \nabla g(\boldsymbol{x},t) - \sigma g(\boldsymbol{x},t) \right) \quad \boldsymbol{x} \in \mathcal{D}^k \quad (36)$$

Fig. 4. Top left, cell cycle division time (45) for $g \in [0.25, 1] \cdot 10^{13}$ kg/mm^3, $\tau = 12$ h and $\bar{g} = 1 \cdot 10^{-13}$; bottom left, branching probability (47) for $g_{br} = \bar{g} = 1 \cdot 10^{-13}$ and $\tau_{br} = 48$ h. On the right representation of the branching directions.

$$D_g \nabla g(\boldsymbol{x}, t) \cdot \boldsymbol{n}_\Gamma^k(\boldsymbol{x}) = -\tilde{\sigma} g(\boldsymbol{x}, t) \qquad \boldsymbol{x} \in \Gamma^k \qquad (37)$$

$$g(\boldsymbol{x}, t) = g^C(\boldsymbol{x}) \qquad \boldsymbol{x} \in \partial C \cap \partial D \qquad (38)$$

$$\nabla g(\boldsymbol{x}, t) \cdot \boldsymbol{n}(\boldsymbol{x}) = 0 \qquad \boldsymbol{x} \in \partial D \setminus (\partial C \cap \partial D) \qquad (39)$$

$$\nabla g(\boldsymbol{x}, t) \cdot \boldsymbol{n}_d^k(\boldsymbol{x}) = 0 \qquad \boldsymbol{x} \in \partial \Sigma_d^k. \qquad (40)$$

For $k = 0$ we set an initial condition

$$g(\boldsymbol{x}, 0) = g_0(\boldsymbol{x}) \qquad \boldsymbol{x} \in D^0.$$

At the interface between the tissue sample and the tumor a constant Dirichlet boundary condition is imposed, modeling a constant distribution g^C of growth factor at the tumor boundary. Parameters D_g and σ are positive scalars denoting respectively the diffusivity of the VEGF and its natural decay rate, $\tilde{\sigma}$ is the rate of consumption of VEGF by endothelial cells. The vector field $\boldsymbol{v}$ is computed according to (10).

Introducing the one-dimensional quantity $\check{g}_i(s, t)$ we neglect the variations of $g(\boldsymbol{x}, t)$ along the cross section perimeter, assuming in cylindrical coordinates, for $s \in (0, S_i^k)$

$$g_{|\Gamma_i^k}(R, \theta, s, t) = \check{g}_i(s, t), \quad \forall \theta \in [0, 2\pi), \ t \in \mathcal{I}_k. \qquad (41)$$

Equations (36)-(37) can thus be reduced to a 3D equation with a singular reaction term

$$\frac{\partial g(\boldsymbol{x}, t)}{\partial t} - \nabla \cdot \left(D_g \nabla g(\boldsymbol{x}, t)\right) + \boldsymbol{v}(\boldsymbol{x}, t) \cdot \nabla g(\boldsymbol{x}, t) + $$
$$ + \sigma g(\boldsymbol{x}, t) = -\sum_{i \in Y^k} 2\pi R \tilde{\sigma} \check{g}(s, t) \delta_{\Lambda_i^k}, \quad \boldsymbol{x} \in D^k, \ t \in \mathcal{I}_k. \qquad (42)$$

The consumption of VEGF by endothelial cells is to be intended in terms of receptor mediated binding, i.e. there is not a flux of VEGF through the vessel wall. For this reason no equation is defined for the concentration of VEGF inside the capillaries.

3.4. The growth of the vascular network

In the following we identify the vascular network at time t_k with its centerline Λ^k and we extend the domain D^k to the whole Ω, with embedded subdomains Λ^k. We denote by $\mathcal{P}^k$ the set of capillary tips at time t_k, being nothing but the centers of the sections $\partial \Sigma_d^k$. We assume that the endothelial cells respond chemotactically to VEGF gradients, undergoing mitosis and producing sprout extension. We model this phenomenon as a displacement of the tip cells, thus monitoring their number and po-

sition. In particular, the position $\boldsymbol{x}_P$ of a generic tip cell $P \in \mathcal{P}^k$ evolves according to

$$\frac{d\boldsymbol{x}_P}{dt} = \boldsymbol{w}(g(\boldsymbol{x}_P, t_k), \boldsymbol{x}_P) \qquad (43)$$

with $\boldsymbol{w}$ denoting the tip velocity and defined, according to [46], as

$$\boldsymbol{w}(g, \boldsymbol{x}) = \begin{cases} \dfrac{l_e}{t_c(g)} \dfrac{\boldsymbol{K}_{ECM}(\boldsymbol{x}) \nabla g}{||\boldsymbol{K}_{ECM}(\boldsymbol{x}) \nabla g||} & \text{if } g \geq g_{lim} \\ 0 & \text{otherwise.} \end{cases} \qquad (44)$$

In the above definition, g_{lim} represents the minimum VEGF concentration for endothelial cell proliferation, i.e. for tip displacement, l_e is the endothelial cell length and t_c is a cell cycle division time, modeled as [46]

$$t_c(g) = \tau \left(1 + e^{\left(\frac{\bar{g}}{g} - 1\right)}\right), \qquad (45)$$

where τ is a cell proliferation parameter, while $\overline{g}$ is the concentration at which $t_c = 2\tau$. In Fig. 4 (top left) function $t_c(g)$ is plotted for $\tau = 12$ h and $\overline{g} = 1 \cdot 10^{-13}$ kg/mm^3. The local orientation of the extracellular matrix (ECM) fibers is modeled through matrix $\boldsymbol{K}_{ECM}$, which is assumed constant in time but variable in space. When no data on the ECM orientation is available, the matrix is defined as $\boldsymbol{K}_{ECM} = \boldsymbol{K}_{ECM}^{rand}$, with

$$\boldsymbol{K}_{ECM}^{rand}(\boldsymbol{x}) = \boldsymbol{I} + k_{an}(\boldsymbol{x}) \boldsymbol{K}_{ECM}^{an}(\boldsymbol{x}). \qquad (46)$$

Matrix $\boldsymbol{K}_{ECM}^{an}(\boldsymbol{x})$ represents deviations from isotropicity and it takes the form

$$\boldsymbol{K}_{ECM}^{an}(\boldsymbol{x}) = \begin{bmatrix} -k_2(\boldsymbol{x})^2 - k_3(\boldsymbol{x})^2 & k_1(\boldsymbol{x})k_2(\boldsymbol{x}) & k_1(\boldsymbol{x})k_3(\boldsymbol{x}) \\ k_1(\boldsymbol{x})k_2(\boldsymbol{x}) & -k_1(\boldsymbol{x})^2 - k_3(\boldsymbol{x})^2 & k_2(\boldsymbol{x})k_3(\boldsymbol{x}) \\ k_1(\boldsymbol{x})k_3(\boldsymbol{x}) & k_2(\boldsymbol{x})k_3(\boldsymbol{x}) & -k_1(\boldsymbol{x})^2 - k_2(\boldsymbol{x})^2 \end{bmatrix}.$$

The parameters $k_i(\boldsymbol{x})$, $i = 1, ..., 3$ and the weight of the anisotropic contribution $k_{an}(\boldsymbol{x})$ are randomly chosen for each position in space, such that $\sum_{i=1}^3 k_i(\boldsymbol{x})^2 = 1$ and $k_{an}(\boldsymbol{x}) \in [0, 1]$. We refer to Section 6.2 for a case in which random perturbation is exploited together with some known features on the ECM orientation.

3.4.1. Branching

In our model the generation of new sprouts from an existing sprout tip (branching) can occur only when the following conditions are both satisfied ([46]):

1. the age of the current sprout is greater than a threshold-age τ_{br}. This means that a time τ_{br} has passed since the sprout last branched;

2. the ratio between the norm of the orthogonal projection of $\boldsymbol{w}$ on the plane perpendicular to the current sprout orientation and the norm of $\boldsymbol{w}$ is greater than a threshold value α_{br}^w.

We introduce also a *branching probability* $P_{br}(g)$, such that branching occurs more probably when the concentration of VEGF is high. The aim of the branching probability function is also to avoid the formation of new branches at a rate which could be incoherently higher than the proliferation rate. According to (45), the cell cycle division time is in fact related to VEGF concentration so that we impose a very low probability of branching when $\tau_{br} < t_c$. In particular we define

$$P_{br}(g) = \begin{cases} e^{-a\left(\frac{g}{g_{br}}-1\right)^4} & \text{if } g < g_{br} \\ 1 & \text{otherwise} \end{cases} \tag{47}$$

with g_{br} corresponding to the VEGF concentration at which the probability of branching is 100%. We choose the parameter a such that the probability of branching is 5% for a value of g corresponding to $t_c = \tau_{br}$. More or less restrictive choices are of course possible, possibly supported by biological experiments. The branching probability function for $g_{br} = \bar{g} = 1.0 \cdot 10^{-13}$ and $\tau_{br} = 48$ h is reported in Fig. 4 (bottom left).

Let $P \in \mathcal{P}^k$ being a sprout tip at time t_k. Let us denote by Π the plane perpendicular to the sprout orientation and by $\boldsymbol{w}_\Pi$ the orthogonal projection of $\boldsymbol{w}(g(\boldsymbol{x}_P, t_k), \boldsymbol{x}_P)$ onto Π. Let us suppose that $\frac{||\boldsymbol{w}_\Pi||}{||\boldsymbol{w}||} > \alpha_{br}^w$ and that the sprout is old enough to branch. If, according to the probability $P_{br}(g(\boldsymbol{x}_P, t_k))$, branching actually occurs, then the directions $\boldsymbol{w}_1$ and $\boldsymbol{w}_2$ of the two new sprouts are obtained as

$$\boldsymbol{w}_1 = \boldsymbol{w} + \frac{\boldsymbol{w}_\Pi}{||\boldsymbol{w}_\Pi||} d_{br}, \qquad \boldsymbol{w}_2 = \boldsymbol{w} - \frac{\boldsymbol{w}_\Pi}{||\boldsymbol{w}_\Pi||} d_{br}$$

with d_{br} denoting the diameter of a single capillary and corresponding to the distance by which the new sprout tips will be separated (see Fig. 4-right).

3.4.2. Anastomosis

Anastomosis, i.e. the formation of loops as a consequence of the fusion of two vessels, is supposed to occur when a sprout tip meets another sprout tip or a portion of a sprout that is not older than a certain threshold-age τ_{an}. Using the nomenclature in [46], the first configuration is called tip-to-tip anastomosis and produces the deactivation of both tips, while the second is called tip-to-sprout and leads only one tip to become inactive. In the simulations, anastomosis is forced when the new sprout tip lies within a distance d_{an} from another tip or from a sufficiently young sprout.

3.5. Summary of model equations

We here provide a summary of the equations involved in the model. The three PDE-problems are written for a generic time interval $\mathcal{I}_k$, for a fixed 1D capillary network Λ^k, $k > 0$. The equation concerning the evolution of the capillary network from Λ_k to Λ^{k+1} is then reported.

Fluid pressure.

$$-\nabla \cdot \left(\frac{\kappa}{\mu} \nabla p(\boldsymbol{x}, t)\right) + \beta_p^{LS} \frac{S}{V} (p(\boldsymbol{x}, t) - p_{LS}) = \sum_{i \in Y^k} \hat{f}_p^i \delta_{\Lambda_i^k} \qquad \boldsymbol{x} \in \mathcal{D}^k$$

$$-\frac{\partial}{\partial s}\left(\frac{\pi R^4}{8\mu} \frac{\partial \hat{p}_i(s,t)}{\partial s}\right) = -\hat{f}_p^i(s,t) \qquad \forall i \in Y^k, \ s \in (0, S_i^k)$$

$$\hat{f}_p^i(s,t) = 2\pi R \beta_p(\hat{p}_i(s,t) - \check{p}_i(s,t) - \Delta p_{onc}) \qquad s \in (0, S_i^k).$$

Oxygen concentration.

$$\frac{\partial c(\boldsymbol{x},t)}{\partial t} - \nabla \cdot \left(D_c \nabla c(\boldsymbol{x},t)\right) + \boldsymbol{v}(\boldsymbol{x},t) \cdot \nabla c(\boldsymbol{x},t) + m_c(c(\boldsymbol{x},t)) = \sum_{i \in Y^k} \hat{f}_c^i \delta_{\Lambda_i^k}$$

$$\boldsymbol{x} \in \mathcal{D}^k$$

$$\pi R^2 \frac{\partial \hat{c}_i(s,t)}{\partial t} - \frac{\partial}{\partial s_i}\left(\pi R^2 \tilde{D}_c \frac{\partial \hat{c}_i(s,t)}{ds}\right) + \pi R^2 \hat{v}_i(s,t) \frac{\partial \hat{c}_i(s,t)}{\partial s_i} = -\hat{f}_c^i(s,t)$$

$$\forall i \in Y^k, \ s \in (0, S_i^k)$$

$$\hat{f}_c^i(s,t) = 2\pi R \beta_c(\hat{c}_i(s,t) - \check{c}_i(s,t)), \quad s \in (0, S_i^k), \ t \in \mathcal{I}_k.$$

VEGF concentration.

$$\frac{\partial g(\boldsymbol{x},t)}{\partial t} - \nabla \cdot \left(D_g \nabla g(\boldsymbol{x},t)\right) + \boldsymbol{v}(\boldsymbol{x},t) \cdot \nabla g(\boldsymbol{x},t) + \tag{48}$$

$$+ \sigma g(\boldsymbol{x},t) = -\sum_{i \in Y^k} 2\pi R \tilde{\sigma} \check{g}(s,t) \delta_{\Lambda_i^k} \quad \boldsymbol{x} \in \mathcal{D}^k.$$

Conditions at bifurcation points.

$$\sum_{j \in Y_b} \frac{\partial \hat{p}_j}{\partial s}(S_{j,b}, t) = 0, \qquad \sum_{j \in Y_b} \frac{\partial \hat{c}_j}{\partial s}(S_{j,b}, t) = 0 \qquad \forall b \in B^k \tag{49}$$

$$\hat{p}_i(S_{i,b}, t) = \hat{p}_j(S_{j,b}, t), \quad \hat{c}_i(S_{i,b}, t) = \hat{c}_j(S_{j,b}, t) \qquad \forall i \neq j \in Y_b, \ \forall b \in B^k. \tag{50}$$

Boundary conditions.

$$\frac{\kappa}{\mu} \nabla p(\boldsymbol{x},t) \cdot \boldsymbol{n}(\boldsymbol{x}) = \beta_p^{ext}(p_{ext} - p(\boldsymbol{x},t)) \qquad \boldsymbol{x} \in \partial D$$

$$D_c \nabla c(\boldsymbol{x},t) \cdot \boldsymbol{n}(\boldsymbol{x}) = \beta_c^{ext}(c_{ext} - c(\boldsymbol{x},t)) \qquad \boldsymbol{x} \in \partial D$$

$$g(\boldsymbol{x},t) = g^C(\boldsymbol{x}) \qquad \boldsymbol{x} \in \partial C \cap \partial D$$

$$\nabla g(\boldsymbol{x},t) \cdot \boldsymbol{n}(\boldsymbol{x}) = 0 \qquad \boldsymbol{x} \in \partial D \setminus (\partial C \cap \partial D)$$

$$\hat{p} = \hat{p}_{in}, \qquad \hat{c} = \hat{c}_{in} \qquad \text{in } \Lambda_{in}$$

$$\hat{p} = \hat{p}_{out}, \qquad \frac{\partial \hat{c}}{\partial s} = 0 \qquad \text{in } \Lambda_{out}$$

$$\frac{\partial \hat{p}}{\partial s} = 0, \qquad \frac{\partial \hat{c}}{\partial s} = 0 \qquad \text{in } \Lambda_d.$$

Initial conditions.

$$c(\boldsymbol{x}, t_0) = c_0(\boldsymbol{x}) \qquad \boldsymbol{x} \in \mathcal{D}^0$$

$$\hat{c}(\boldsymbol{x}, t_0) = \hat{c}_0(\boldsymbol{x}) \qquad \boldsymbol{x} \in \Lambda^0$$

$$\hat{c}(\boldsymbol{x}, t_{k-1}) = 0 \qquad \boldsymbol{x} \in \Lambda^k \setminus \Lambda^{k-1}$$

$$g(\boldsymbol{x}, 0) = g_0(\boldsymbol{x}) \qquad \boldsymbol{x} \in \mathcal{D}^0.$$

Tip cell movement. $\quad \forall P \in \mathcal{P}^k$

$$\frac{d\boldsymbol{x}_P}{dt} = \begin{cases} \dfrac{l_e}{t_c(g(\boldsymbol{x}_P, t_k))} \dfrac{\boldsymbol{K}_{ECM}(\boldsymbol{x}_P) \nabla g(\boldsymbol{x}_P, t_k)}{||\boldsymbol{K}_{ECM}(\boldsymbol{x}_P) \nabla g(\boldsymbol{x}_P, t_k)||} & \text{if } g(\boldsymbol{x}_P, t_k) \geq g_{lim} \\ 0 & \text{otherwise.} \end{cases}$$

4. The optimization based domain decomposition for 3D-1D coupling

The problems of pressure and oxygen concentration require a coupling between a 3D and a 1D problem. Providing a well-posed mathematical formulation for this kind of coupling is not trivial, since no bounded trace operator is defined when the dimensionality gap between the interested manifolds is higher than one. However it is possible to define suitable subspaces of the Sobolev spaces typically employed for the variational formulation of partial differential equations, in which the definition of such a trace operator is never required. After having defined the proper spaces in which to look for the solutions we aim at applying the optimization based 3D-1D coupling strategy presented in [72]. This choice is related to the fact that this approach has no mesh conformity requirements and, hence, it allows to easily handle complex time-varying geometries as the ones characterizing angiogenesis simulations. We refer to [71]-[72] for a wider presentation of the method, while trying to give the main ideas in the following. In this section we focus on problem (32)-(35) in which time derivation, advection and

reaction contributions are present. The same considerations hold, however, for more simple elliptic problems as (15)-(18).

Let us consider $t \in \mathcal{I}_k = (t_{k-1}, t_k]$ and let us define the space

$$H^1(\Lambda^k) = \prod_{i \in Y^k} H^1(\Lambda_i^k) \cap C^0(\Lambda^k),$$

being nothing but the space of continuous functions on Λ^k whose restriction to Λ_i^k is in $H^1(\Lambda_i^k)$. Each function $\hat{u} \in H^1(\Lambda^k)$ can be written as

$$\hat{u} = \prod_{i \in Y^k} \hat{u}_i, \quad \hat{u}_i \in H^1(\Lambda_i^k).$$

More in general, in the remainder of this section, we denote by w_i the restriction of a sufficiently regular function w to Λ_i^k. We then define a trace operator

$$\gamma_i^k : H^1(D^k) \cup H^1(\Sigma_i^k) \to H^{\frac{1}{2}}(\Gamma_i^k)$$

which, given $u \in H^1(D^k) \cup H^1(\Sigma^k)$, returns $\gamma_i^k u = u_{|_{\Gamma_i^k}}$ $i \in Y^k$, and an extension operator

$$\mathcal{E}_i^k : H^1(\Lambda_i^k) \to H^{\frac{1}{2}}(\Gamma_i^k)$$

which, given $\hat{u}_i \in H^1(\Lambda_i^k)$ uniformly extends the value $\hat{u}_i(s)$ to the boundary $\Gamma_i^k(s)$ of the transversal section $\Sigma_i^k(s)$, i.e. $\mathcal{E}_i^k \hat{u}_i(s) = \tilde{u}(\boldsymbol{x}) \forall \boldsymbol{x} \in \Gamma_i^k(s)$. Then, we define

$$\hat{V}_0^k = \left\{ \hat{u} \in H^1(\Lambda^k) : \hat{u}_{|_{\Lambda_{in}}} = 0 \right\}, \quad \hat{V}^k = \left\{ \hat{u} \in H^1(\Lambda^k) : \hat{u}_{|_{\Lambda_{in}}} = \hat{c}_{in} \right\},$$

with Λ_{in} collecting the centers of the inflow sections $\partial \Sigma_{in}$, and

$$\mathcal{H}_i^{\Gamma^k} = \{ u \in H^{\frac{1}{2}}(\Gamma_i^k) : u = \mathcal{E}_i^k \hat{u}_i, \ \hat{u} \in \hat{V}^k \}$$

$$V^k = \left\{ u \in H^1(D^k) : \gamma_i^k u \in \mathcal{H}_i^{\Gamma^k}, \ \forall i \in Y^k \right\}.$$

Also, the space $\widetilde{V}_i^k$ is introduced as:

$$\widetilde{V}_i^k = \{ u \in H^1(\Sigma_i^k) : u = \Xi_i^k \hat{u}_i, \ \hat{u} \in \hat{V}^k \},$$

where $\Xi_i^k : H^1(\Lambda_i^k) \to H^1(\Sigma_i^k)$ is an extension operator which uniformly extends the value $\hat{u}_i(s)$ to the cross section $\Sigma_i^k(s)$ of the cylinder, i.e. $\Xi_i^k \hat{u}_i(s) = \tilde{u}(\boldsymbol{x}) \forall \boldsymbol{x} \in \Sigma_i^k(s)$.

According to (29)-(30) we choose, $\forall t \in \mathcal{I}_k$

$$c(t) \in V^k \quad \text{and} \quad \tilde{c}(t) = \prod_{i \in Y^k} \tilde{c}_i(t), \ \tilde{c}_i(t) \in \widetilde{V}_i^k.$$

We denote by $\check{c}(t) \in \hat{V}^k$ the function such that $\gamma_i^k c(t) = \mathcal{E}_i^k \check{c}_i(t)$, as in (30), and similarly by $\hat{c}(t) \in \hat{V}^k$ the function such that $\tilde{c}(t)(\boldsymbol{x}) = \Xi_i^k \hat{c}_i(t)$ $\forall \boldsymbol{x} \in \Sigma_i^k$.

The 3D-1D variational formulation of problem (32)-(35) can now be written as: $\forall t \in \mathcal{I}_k$, find $c(t) \in V^k$, $\hat{c}(t) \in \hat{V}^k$ such that

$$\left(\frac{\partial c}{\partial t}, \eta \right)_{L^2(D^k)} + \left(D_c \nabla c, \nabla \eta \right)_{L^2(D^k)} + \left(\boldsymbol{v} \cdot \nabla c, \eta \right)_{L^2(D^k)} + \left(M_c c, \eta \right)_{L^2(D^k)} +$$

$$+ (\beta_c^{ext} c, \eta)_{L^2(\partial D)} + \sum_{i \in Y^k} (2\pi R \beta_c (\check{c}_i - \hat{c}_i), \check{\eta}_i)_{L^2(\Lambda_i^k)} =$$

$$= (\beta_c^{ext} c_{ext}, \eta)_{L^2(\partial D)} \qquad \forall \eta \in V^k : \gamma_i^k \eta = \mathcal{E}_i^k \check{\eta}_i, \check{\eta} \in \hat{V}_0^k \tag{51}$$

$$\sum_{i \in Y^k} \left[\left(\pi R^2 \frac{\partial \hat{c}_i}{\partial t}, \hat{\eta}_i \right)_{L^2(\Lambda_i^k)} + \left(\pi R^2 \tilde{D}_c \frac{\partial \hat{c}_i}{\partial s}, \frac{\partial \hat{\eta}_i}{\partial s} \right)_{L^2(\Lambda_i^k)} + \right.$$

$$\left. + \left(\pi R^2 \hat{v}_i \frac{\partial \hat{c}_i}{\partial s}, \hat{\eta}_i \right)_{L^2(\Lambda_i^k)} + \left(2\pi R \beta_c (\hat{c}_i - \check{c}_i), \hat{\eta}_i \right)_{L^2(\Lambda_i^k)} \right] = 0 \qquad \forall \hat{\eta} \in \hat{V}_0^k. \tag{52}$$

As mentioned before, we now aim at applying the optimization based 3D-1D coupling approach presented in [72]. The method resorts to a domain decomposition strategy, in which two auxiliary variables are introduced at the interface in order to decouple the problems defined in the vascular network and in the surrounding tissue. We denote

such variables by $\hat{\psi}^D(t)$ and $\hat{\psi}^\Sigma(t)$ and we rewrite problem (51)-(52) as: $\forall t \in \mathcal{I}_k$, find $c(t) \in V^k$, $\hat{c}(t) \in \hat{V}_c^k$, $\hat{\psi}^D(t) \in \hat{V}^k$, $\hat{\psi}^\Sigma(t) \in \hat{V}^k$ such that

$$\left(\frac{\partial c}{\partial t}, \eta \right)_{L^2(D^k)} + \left(D_c \nabla c, \nabla \eta \right)_{L^2(D^k)} + \left(\boldsymbol{v} \cdot \nabla c, \eta \right)_{L^2(D^k)} + \left(M_c c, \eta \right)_{L^2(D^k)} +$$

$$+ (\beta_c^{ext} c, \eta)_{L^2(\partial D)} + \sum_{i \in Y^k} (2\pi R \beta_c \check{c}_i, \check{\eta}_i)_{L^2(\Lambda_i^k)} - \sum_{i \in Y^k} (2\pi R \beta_c \hat{\psi}_i^\Sigma, \check{\eta}_i)_{L^2(\Lambda_i^k)} =$$

$$= (\beta_c^{ext} c_{ext}, \eta)_{L^2(\partial D)}, \qquad \forall \eta \in V^k : \gamma_i^k \eta = \mathcal{E}_i^k \check{\eta}_i, \check{\eta} \in \hat{V}_0^k \tag{53}$$

$$\sum_{i \in Y^k} \left[\left(\pi R^2 \frac{\partial \hat{c}_i}{\partial t}, \hat{\eta}_i \right)_{L^2(\Lambda_i^k)} + \left(\pi R^2 \tilde{D}_c \frac{\partial \hat{c}_i}{\partial s}, \frac{\partial \hat{\eta}_i}{\partial s} \right)_{L^2(\Lambda_i^k)} + \right.$$

$$\left. + \left(\pi R^2 \hat{v}_i \frac{\partial \hat{c}_i}{\partial s}, \hat{\eta}_i \right)_{L^2(\Lambda_i^k)} + \left(2\pi R \beta_c \hat{c}_i, \hat{\eta}_i \right)_{L^2(\Lambda_i^k)} - (2\pi R \beta_c \hat{\psi}_i^D, \hat{\eta}_i)_{L^2(\Lambda_i^k)} \right]$$

$$= 0, \qquad \forall \hat{\eta} \in \hat{V}_0^k \tag{54}$$

with interface conditions, $\forall i \in Y^k$,

$$\left\langle \check{c}_i(t) - \hat{\psi}_i^D(t), \hat{\mu}_i \right\rangle_{\hat{V}_0^k, \hat{V}_0^{k'}} = 0 \qquad \forall \hat{\mu}_i \in \hat{V}_0^{k'}, \ t \in \mathcal{I}_k, \tag{55}$$

$$\left\langle \hat{c}_i(t) - \hat{\psi}_i^\Sigma(t), \hat{\mu}_i \right\rangle_{\hat{V}_0^k, \hat{V}_0^{k'}} = 0 \qquad \forall \hat{\mu}_i \in \hat{V}_0^{k'}, \ t \in \mathcal{I}_k. \tag{56}$$

The final step is to recast our problem into a PDE-constrained optimization problem. We hence introduce a cost functional, which mimics the error committed by approximating $\check{c}(t)$ and $\hat{c}(t)$ by $\hat{\psi}^D(t)$ and $\hat{\psi}^\Sigma(t)$ respectively:

$$J^k(\hat{\psi}^D(t), \hat{\psi}^\Sigma(t)) = \frac{1}{2} \sum_{i \in Y^k} \left(||\check{c}_i(t) - \hat{\psi}_i^D(t)||_{L^2(\Lambda_i^k)}^2 + ||\hat{c}_i(t) - \hat{\psi}_i^\Sigma(t)||_{L^2(\Lambda_i^k)}^2 \right). \tag{57}$$

The variational PDE-constrained optimization formulation of problem (19)-(28) finally reads: $\forall t \in \mathcal{I}_k$

$$\min_{\hat{\psi}^D(t), \hat{\psi}^\Sigma(t) \in \hat{V}^k} J^k(\hat{\psi}^D(t), \hat{\psi}^\Sigma(t)) \text{ subject to (53)-(54).} \tag{58}$$

Handling the 3D-1D coupled problem as an optimization problem ends up in a method for which no mesh conformity is required. This represents a great advantage in angiogenesis simulations, since we will never need to remesh the tissue as the vascular network grows. Further, interface quantities are directly computed, without any need of post processing. We refer to Section 5 for details about meshes and for the discretization of problem (58).

As previously mentioned, the problem for VEGF is a 3D problem with singular sink term, since there is no VEGF flux through the vessel wall. Hence we do not need to deal with a 3D-1D coupled problem. However we here report the variational formulation of Equation (42) which will be used in Section 5 to derive the discrete matrix formulation. Let us introduce the spaces

$$V_{0^c}^k = \left\{ u \in H^1(D^k) : \gamma_i^k u \in \mathcal{H}_i^{\Gamma^k} \text{ and } u_{|_{\partial D \cap \partial C}} = 0 \right\},$$

$$V_{g^c}^k = \left\{ u \in H^1(D^k) : \gamma_i^k u \in \mathcal{H}_i^{\Gamma^k} \text{ and } u_{|_{\partial D \cap \partial C}} = g^C \right\}.$$

The variational problem then reads: Find $g(t) \in V_{g^c}^k$ such that

$$\begin{cases} \left(\partial_t g, \eta \right)_{L^2(D^k)} + \left(D_g \nabla g, \nabla \eta \right)_{L^2(D^k)} + \left(\boldsymbol{v} \cdot \nabla g, \eta \right)_{L^2(D^k)} + \left(\sigma g, \eta \right)_{L^2(D^k)} + \\ \quad + \sum_{i \in Y^k} \left(2\pi R \tilde{\sigma} \check{g}_i, \check{\eta}_i \right)_{L^2(\Lambda_i^k)} = 0 \quad \forall \eta \in V_{0^c}^k : \gamma_i^k \eta = \mathcal{E}_i^k \check{\eta}, \check{\eta} \in H^1(\Lambda^k) \\ g(0) = g_0 \end{cases} \tag{59}$$

where $\gamma_i^k g(t) = \mathcal{E}_i^k \check{g}_i(t)$.

5. Problem discretization

Here the discretization of the equations reported in Section 4 is provided. We start from the problem for oxygen concentration, resulting from the application of the optimization method, then we move to the

VEGF problem and to the network growth. The discretization of the pressure problem can be easily derived from the steps made for oxygen concentration.

5.1. The discrete optimization problem

As already mentioned in Section 3.4, for the discretization of the 3D-1D coupled problems, the 3D domain is extended to the whole Ω. Let us consider a tetrahedral mesh $\mathcal{T}$ on domain Ω, independent from the position of the vessel network. Denoting by N the number of DOFs for oxygen inside Ω, let us define linear Lagrangian basis functions $\{\varphi_j\}_{j=1}^{N}$ such that the discrete approximation of $c(t)$ is $C(t) = \sum_{j=1}^{N} C_j(t)\varphi_k$. For what concerns the 1D variables, we build on Λ^k three different partitions $\hat{\mathcal{T}}^k$, τ_D^k and τ_Σ^k, independent from each other and from $\mathcal{T}$. Such meshes could change at each time-step, but, for computational efficiency we choose to incrementally add mesh elements as the network grows. To ensure mesh uniformity, a minimum element size can be fixed, such that new mesh elements are created only if larger than the minimum size. We define the basis functions $\{\hat{\varphi}_j\}_{j=1}^{\hat{N}^k}$ on $\hat{\mathcal{T}}^k$, $\left\{\theta_j^D\right\}_{j=1}^{\hat{N}_D^k}$ on τ_D^k and $\left\{\theta_j^\Sigma\right\}_{j=1}^{\hat{N}_\Sigma^k}$ on τ_Σ^k, with $\hat{N}^k$, $\hat{N}_D^k$ and $\hat{N}_\Sigma^k$ denoting the number of DOFs at time t_k of the discrete approximations of the variables $\hat{c}(t)$, $\hat{\psi}^D(t)$ and $\hat{\psi}^\Sigma(t)$. We remark that the basis functions do not depend on time, only their number can vary with time. The approximations of $\hat{c}(t)$, $\hat{\psi}^D(t)$ and $\hat{\psi}^\Sigma(t)$ on the vascular network Λ_k are defined as:

$$\hat{C}(t) = \sum_{j=1}^{\hat{N}^k} \hat{C}_j(t)\,\hat{\varphi}_j, \quad \Psi^D(t) = \sum_{j=1}^{\hat{N}_D^k} \Psi_j^D(t)\,\theta_j^D, \quad \Psi^\Sigma(t) = \sum_{j=1}^{\hat{N}_\Sigma^k} \Psi_j^\Sigma(t)\,\theta_j^\Sigma.$$

Let us now define the matrices

$$\boldsymbol{A}^k \in \mathbb{R}^{N\times N} \text{ s.t. } A_{lj}^k = \int_\Omega \left(D_c \nabla\varphi_j \cdot \nabla\varphi_l + (\boldsymbol{v}\cdot\nabla\varphi_j)\varphi_l + m_c\varphi_j\varphi_l \right)\, d\omega +$$

$$+ \int_{\partial\Omega} \beta_c^{ext}\varphi_{j|_{\partial\Omega}}\varphi_{l|_{\partial\Omega}} d\sigma + \int_{\Lambda^k} 2\pi R\beta_c\varphi_{j|_{\Lambda^k}}\varphi_{l|_{\Lambda^k}}\, ds,$$

$$\hat{\boldsymbol{A}}^k \in \mathbb{R}^{\hat{N}^k\times\hat{N}^k} \text{ s.t. } \hat{A}_{lj}^k = \int_{\Lambda^k} \left(\pi R^2 \tilde{D}_c \frac{d\hat{\varphi}_j}{ds}\frac{d\hat{\varphi}_l}{ds} + \pi R^2 \hat{v}\frac{d\hat{\varphi}_j}{ds}\hat{\varphi}_l \right)\, ds +$$

$$+ \int_{\Lambda^k} 2\pi R\beta_c\hat{\varphi}_j\hat{\varphi}_l\, ds$$

$$\boldsymbol{M} \in \mathbb{R}^{N\times N} \text{ s.t. } M_{lj} = \int_\Omega \varphi_j\varphi_l\, d\omega$$

$$\hat{\boldsymbol{M}}^k \in \mathbb{R}^{\hat{N}^k\times\hat{N}} \text{ s.t. } \hat{M}_{lj}^k = \int_{\Lambda^k} \pi R^2\hat{\varphi}_j\hat{\varphi}_l\, ds,$$

$$\hat{\boldsymbol{D}}_\beta^k \in \mathbb{R}^{\hat{N}^k\times\hat{N}_D^k} \text{ s.t. } (\hat{D}_\beta^k)_{lj} = \int_{\Lambda^k} 2\pi R\beta_c\hat{\varphi}_l\,\theta_j^D\, ds,$$

$$\boldsymbol{S}_\beta^k \in \mathbb{R}^{N\times\hat{N}_\Sigma^k} \text{ s.t. } (S_\beta^k)_{lj} = \int_{\Lambda^k} 2\pi R\beta_c\varphi_{l|_{\Lambda^k}}\theta_j^\Sigma\, ds$$

and the vector

$$F \in \mathbb{R}^N \text{ s.t. } F_l = \int_{\partial\Omega} \beta_c^{ext}c_{ext}\varphi_l\, d\sigma.$$

The implicit Euler scheme is adopted for time-discretization. At this aim let us define a uniform partition of the time interval $\mathcal{I}_k$ with a step $\Delta t \leq \Delta\mathcal{I}_k$ and $t_{k,q} = t_{k-1} + q\Delta t$, $q \geq 0$. The fully discretized version of equations (53)-(54) then reads:

$$\begin{cases} \left(\boldsymbol{M} + \Delta t\boldsymbol{A}^k\right)C(t_{k,q}) - \Delta t\boldsymbol{S}_\beta^k\Psi_\Sigma(t_{k,q}) = \boldsymbol{M}C(t_{k,q-1}) + \Delta tF \\ \left(\hat{\boldsymbol{M}}^k + \Delta t\hat{\boldsymbol{A}}^k\right)\hat{C}(t_{k,q}) - \Delta t\hat{\boldsymbol{D}}_\beta^k\Psi_D(t_{k,q}) = \hat{\boldsymbol{M}}^k\hat{C}(t_{k,q-1}) \\ C(t_{k,0}) = \begin{cases} C_0 & \text{if } k = 0 \\ C(t_{k-1}) & \text{if } k > 0 \end{cases} \\ \hat{C}(t_{k,0}) = \begin{cases} \hat{C}_0 & \text{if } k = 0 \\ \hat{C}_\sharp(t_{k-1}) & \text{if } k > 0 \end{cases} \end{cases} \tag{60}$$

where $\hat{C}_\sharp(t_{k-1})$ is the trivial extension of $\hat{C}(t_{k-1}) \in \mathbb{R}^{\hat{N}^{k-1}}$ to $\mathbb{R}^{\hat{N}^k}$ by zero elements in correspondence of DOFs defined on $\Lambda^k \setminus \Lambda^{k-1}$.

In order to work out the discrete formulation of functional (57) let us build the matrices

$$\boldsymbol{G}^k \in \mathbb{R}^{N\times N} \text{ s.t. } G_{lj}^k = \int_{\Lambda^k} \varphi_{j|_{\Lambda^k}}\varphi_{l|_{\Lambda^k}}\, ds,$$

$$\hat{\boldsymbol{G}}^k \in \mathbb{R}^{\hat{N}^k\times\hat{N}^k} \text{ s.t. } \hat{G}_{lj}^k = \int_{\Lambda^k} \hat{\varphi}_j\,\hat{\varphi}_l\, ds,$$

$$\boldsymbol{D}^k \in \mathbb{R}^{N\times\hat{N}_D^k} \text{ s.t. } D_{lj}^k = \int_{\Lambda^k} \varphi_{l|_{\Lambda^k}}\,\theta_j^D\, ds,$$

$$\hat{\boldsymbol{S}}^k \in \mathbb{R}^{\hat{N}^k\times\hat{N}_\Sigma^k} \text{ s.t. } \hat{S}_{lj}^k = \int_{\Lambda^k} \hat{\varphi}_l\,\theta_j^\Sigma\, ds,$$

$$\boldsymbol{G}_D^k \in \mathbb{R}^{\hat{N}_D^k\times\hat{N}_D^k} \text{ s.t. } (G_D^k)_{lj} = \int_{\Lambda^k} \theta_j^D\,\theta_l^D\, ds,$$

$$\boldsymbol{G}_\Sigma^k \in \mathbb{R}^{\hat{N}_\Sigma^k\times\hat{N}_\Sigma^k} \text{ s.t. } (G_\Sigma^k)_{lj} = \int_{\Lambda^k} \theta_j^\Sigma\,\theta_l^\Sigma\, ds.$$

The discrete cost functional at time $t_{k,q}$ then reads:

$$\tilde{J}^{k,q} = \frac{1}{2}\Big(C(t_{k,q})^T\boldsymbol{G}^kC(t_{k,q}) - C(t_{k,q})^T\boldsymbol{D}^k\Psi_D(t_{k,q}) - \Psi_D(t_{k,q})^T(\boldsymbol{D}^k)^TC(t_{k,q}) +$$

$$+ \Psi_D(t_{k,q})^T\boldsymbol{G}_D^k\Psi_D(t_{k,q}) + \hat{C}(t_{k,q})^T\hat{\boldsymbol{G}}^k\hat{C}(t_{k,q}) - \hat{C}(t_{k,q})^T\hat{\boldsymbol{S}}^k\Psi_\Sigma(t_{k,q}) +$$

$$- \Psi_\Sigma(t_{k,q})^T(\hat{\boldsymbol{S}}^k)^T\hat{C}(t_{k,q}) + \Psi_\Sigma(t_{k,q})^T\boldsymbol{G}_\Sigma^k\Psi_\Sigma(t_{k,q})\Big). \tag{61}$$

Introducing the matrices

$$\mathcal{G}^k = \begin{bmatrix} \boldsymbol{G}^k & 0 & -\boldsymbol{D}^k & 0 \\ 0 & \hat{\boldsymbol{G}}^k & 0 & -\hat{\boldsymbol{S}}^k \\ -(\boldsymbol{D}^k)^T & 0 & \boldsymbol{G}_D^k & 0 \\ 0 & -(\hat{\boldsymbol{S}}^k)^T & 0 & \boldsymbol{G}_\Sigma^k \end{bmatrix}$$

$$\mathcal{A}^k = \begin{bmatrix} \boldsymbol{A}^k & 0 \\ 0 & \hat{\boldsymbol{A}}^k \end{bmatrix}, \quad \mathcal{M}^k = \begin{bmatrix} \boldsymbol{M} & 0 \\ 0 & \hat{\boldsymbol{M}}^k \end{bmatrix}, \quad \mathcal{C}_\beta^k = \begin{bmatrix} 0 & \boldsymbol{S}_\beta^k \\ \boldsymbol{D}_\beta^k & 0 \end{bmatrix},$$

$$\mathcal{A}_{\Delta t}^k = \begin{bmatrix} \Delta t\mathcal{A}^k + \mathcal{M}^k & -\Delta t\mathcal{C}_\beta^k \end{bmatrix}$$

first order optimality conditions for the minimization of (61) constrained by Equations (60) are collected in the saddle-point system

$$\mathcal{K}^k = \begin{bmatrix} \mathcal{G}^k & (\mathcal{A}_{\Delta t}^k)^T \\ \mathcal{A}_{\Delta t}^k & 0 \end{bmatrix}$$

$$\mathcal{K}^k \begin{bmatrix} C(t_k) \\ \hat{C}(t_{k,q}) \\ \Psi_D(t_{k,q}) \\ \Psi_\Sigma(t_{k,q}) \\ -\Pi(t_{k,q}) \\ -\hat{\Pi}(t_{k,q}) \end{bmatrix} = \begin{bmatrix} 0 \\ 0 \\ 0 \\ 0 \\ \boldsymbol{M}C(t_{k,q-1}) + \Delta tF \\ \hat{\boldsymbol{M}}^k\hat{C}(t_{k,q-1}) \end{bmatrix} \tag{62}$$

which is solved at each time-step δt. Vectors Π and $\hat{\Pi}$ are the vector of DOFs of Lagrange multipliers. Let us observe that, by a proper organization of the DOFs, most matrices do not need to be rebuilt completely at each k: only the integrals on $\Lambda^k \setminus \Lambda^{k-1}$ have to be computed and properly concatenated to the matrices already available at time t_{k-1}. Only

the matrices $\boldsymbol{A}$ and $\hat{\boldsymbol{A}}$ need a further update, in order to account for the variation of the velocity field. This update affects however only the advection contribution to such matrices. For the proof of the uniqueness of the solution to (62) we refer to [72].

5.2. The discrete problem for VEGF and capillary growth

The finite element discretization of Problem (59) is obtained considering a tetrahedral mesh $\mathcal{T}$ on domain Ω and defining on it linear Lagrangian basis functions $\{\varphi_j\}_{j=1}^{N_G}$, such that $G(t) = \sum_{j=1}^{N_G} G_k(t)\varphi_j$ is the discrete approximation of variable $g(t)$ being N_G the number of degrees of freedom. We then define the matrices

$$\boldsymbol{B}^k \in \mathbb{R}^{N_G \times N_G} \text{ s.t. } B_{lj}^k = \int_\Omega D_g \nabla\varphi_j \cdot \nabla\varphi_l \, d\omega + \int_\Omega (\boldsymbol{v} \cdot \nabla\varphi_j)\varphi_l \, d\omega +$$

$$+ \int_\Omega \sigma\varphi_j\varphi_l \, d\omega + \int_{\Lambda^k} 2\pi R\tilde{\sigma}\varphi_{j|\Lambda^k}\varphi_{l|\Lambda^k} \, ds$$

$$\boldsymbol{H} \in \mathbb{R}^{N_G \times N_G} \text{ s.t. } H_{lj} = \int_\Omega \varphi_j\varphi_l \, d\omega$$

such that the space semi-discretization of problem (59) reads

$$\begin{cases} \boldsymbol{H}G'(t) + \boldsymbol{B}^k G(t) = 0 & t \in \mathcal{I}_k \\ G(0) = G_0 \end{cases} \tag{63}$$

with $G' = \partial_t G$. For what concerns time discretization we adopt an implicit Euler scheme, considering again a uniform partition of $\mathcal{I}_k$ with $\Delta t \leq \Delta \mathcal{I}_k$ and $t_{k,q} = t_{k-1} + q\Delta t$ we solve at each time step a system in the form

$$\begin{cases} (\boldsymbol{H} + \Delta t\boldsymbol{B}^k) G(t_{k,q}) = \boldsymbol{H}G(t_{k,q-1}) & k > 0 \\ G(t_{k,0}) = \begin{cases} G_0 & \text{if } k = 0 \\ G(t_{k-1}) & \text{if } k > 0. \end{cases} \end{cases} \tag{64}$$

For what concerns Equation (43), discretization is made by the explicit Euler method. Once the VEGF concentration at time t_k has been computed, the position of the tip cells is updated as

$$\boldsymbol{x}_P(t_{k+1}) = \boldsymbol{x}_P(t_k) + \Delta\mathcal{I}_{k+1} \cdot \boldsymbol{w}(G(t_k), \boldsymbol{x}_P(t_k)), \quad \forall P \in \mathcal{P}^k \tag{65}$$

providing the position of a tip cell in $\mathcal{P}^{k+1}$. The points $\boldsymbol{x}_P(t_{k+1})$ and $\boldsymbol{x}_P(t_k)$ are then connected by a line, such that the capillary network is represented by sets of connected segments in the 3D space. In case branching occurs, the orthogonal projection $\boldsymbol{w}_\Pi$ of $\boldsymbol{w}(G(t_k), \boldsymbol{x}_P(t_k))$ onto the plane Π perpendicular to the direction $\boldsymbol{x}_P(t_k) - \boldsymbol{x}_P(t_{k-1})$ has to be computed in order to obtain the branching directions $\boldsymbol{w}_1$ and $\boldsymbol{w}_2$. Equation (65) is then split into

$$\boldsymbol{x}_P^1(t_{k+1}) = \boldsymbol{x}_P(t_k) + \Delta\mathcal{I}_{k+1}\boldsymbol{w}_1, \qquad \boldsymbol{x}_P^2(t_{k+1}) = \boldsymbol{x}_P(t_k) + \Delta\mathcal{I}_{k+1}\boldsymbol{w}_2 \tag{66}$$

producing two new sprout tips. Once the new positions of the tip cells have been computed, the network is updated as

$$\Lambda^{k+1} = \Lambda^k \cup \bigcup_{\substack{P \in \mathcal{P}^k \\ i=1,2}} [x_P^i(t_{k+1}), x_P(t_k)]$$

which is the fixed geometry on which the other quantities will evolve for $t \in \mathcal{I}_{k+1}$.

6. Numerical experiments

In this section we provide some numerical examples exploiting the previously proposed approach. For the numerical validation of the optimization based 3D-1D coupling strategy we refer the reader to [71] and [72], in which considerations on the accuracy and the efficacy of the method are reported for simpler test cases. In the present work we focus instead on two test cases, labeled *TestFace* and *TestSphere*. In the first case the domain Ω is a cube and the tumor interface corresponds

Table 1
Default parameters for the geometry.

Parameter	Value	Unit	Description	Reference
L	$0.5 - 2.5$	mm	Domain edge length	[5,74,75]
R	$5 \cdot 10^{-3}$	mm	Vessel radius	[76]

to one of its faces. A small initial vascular network with two inlet and two outlet points is considered, located at the opposite of the tumor interface, as shown in Fig. 5-left. For the second test the tumor is instead supposed to be spherical and located at the center of a cubic domain. For this case a more complex initial network is considered, as reported in Fig. 5-right. In the following we choose $\Delta t = \Delta\mathcal{I}_k$, i.e. we consider the same, uniform, time-stepping for the growth of the network and for the evolution on the quantities defined on it.

Tables 1-4 provide a set of parameter values to which we will refer as *default parameters*. Changes to these values will be specified and motivated on a case-by-case basis. The parameter values for pressure and oxygen concentration are mainly taken from [51]. For what concerns the VEGF, in [77] its concentration is assumed to be at a constant value of 20 ng/ml, while in [78] endothelial cells are stimulated to migrate with a VEGF concentration of 50 ng/ml. Converting to the units of measure used in the numerical simulations, the order of magnitude of concentrations is of 10^{-14} kg/mm³. We choose $g_{lim} = 2.5 \cdot 10^{-14}$ kg/mm³ and, according to [46] we set $\overline{g} = 4g_{lim} = 1 \cdot 10^{-13}$ kg/mm³ in Equation (45). At the tumor interface we fix $g^C = 10^{-13}$ kg/mm³, so that the cell proliferation time t_c in the simulation will be in the range $(2\tau, +\infty)$. The diffusion coefficient inferred from biological data, for the vast majority of angiogenic growth factors, is in the order of $10 - 600$ μm²/s [23,42,79], i.e. between 0.036 and 2.16 mm²/h, while the decay rate of the VEGF in the surrounding tissue is in the order of $0.456 - 0.65$ h^{-1} [79,80].

The initial distributions of pressure, oxygen and VEGF are obtained solving respectively problems (1)-(9), (19)-(28) and (36)-(40) in steady state conditions. In the numerical simulations the initial set of vessels is supposed, at all time instants, to have a lower permeability with respect to the ones generated during angiogenesis. This is in accordance with the biological observation that tumor-induced vessels are highly leaky, due to a weakening of the junctions between the endothelial cells that leads to an increase in the permeability of the blood vessel [15] both to fluids, oxygen and other nutrients. In particular we suppose

$$\beta_p(\boldsymbol{x}) = \begin{cases} \beta_p^0 & \forall \boldsymbol{x} \in \Lambda^0 \\ r_p^\beta \beta_p^0 & \forall \boldsymbol{x} \in \Lambda^k \setminus \Lambda^0, \, \forall k = 0, ..., K \end{cases} \tag{67}$$

and

$$\beta_c(\boldsymbol{x}) = \begin{cases} \beta_c^0 & \forall \boldsymbol{x} \in \Lambda^0 \\ r_c^\beta \beta_c^0 & \forall \boldsymbol{x} \in \Lambda^k \setminus \Lambda^0, \, \forall k = 0, ..., K, \end{cases} \tag{68}$$

with $r_p^\beta, r_c^\beta \geq 1$. In the default set of parameters we consider $r_p^\beta = 100$ and $r_c^\beta = 10$. The fact that the permeability of vessels to fluids increases by two order of magnitude in tumor-induced vessels is in agreement with [50]. Different choices of the ratio r_c^β will instead be discussed in the sensitivity analysis carried out in this section. Finally, we suppose that only stalk and tip cells can bind VEGF, so that

$$\tilde{\sigma}(\boldsymbol{x}) = \begin{cases} 0 & \forall \boldsymbol{x} \in \Lambda^0, \\ \tilde{\sigma} & \forall \boldsymbol{x} \in \Lambda^k \setminus \Lambda^0, \, \forall k = 0, ..., K. \end{cases}$$

6.1. TestFace

Let us consider a cubic domain $\Omega = (0, L)^3$, $L = 0.5$ mm. The interface between the tumor and the tissue sample corresponds to the top face of Ω, highlighted in red in Fig. 5-left, while the blood inlet and outlet points on the initial network are marked in red and blue respectively. For the time discretization we choose a step $\Delta t = \Delta\mathcal{I}_k = 12$ h
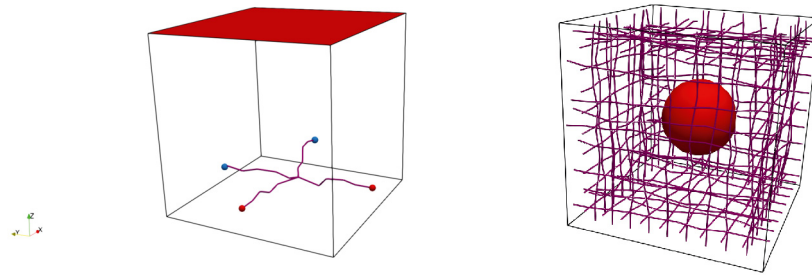
Fig. 5. Initial configurations for the proposed numerical experiments, on the left *TestFace* (inlet and outlet extrema in red and blue respectively), on the right *TestSphere*.

Table 2
Default parameters for pressure.

Parameter	Value	Unit	Description	Reference
β_p^0	$2.78 \cdot 10^{-10}$	$\frac{mm^2 h}{kg}$	Hydraulic permeability of healthy capillary wall	[51]
r_p^β	100	–	Increase of wall permeability for tumor-generated capillaries	[50]
Δp_{onc}	$4.82 \cdot 10^7$	$\frac{kg}{h^2 mm}$	Oncotic pressure jump at the capillary wall	[51]
$\beta_p^{LS} \frac{S}{V}$	$2.89 \cdot 10^{-7}$	$\frac{mm\,h}{kg}$	Effective permeability of the lymphatic vessels	[51,48]
κ	$1.0 \cdot 10^{-12}$	mm^2	Hydraulic permeability of the tissue	[51]
μ	$1.44 \cdot 10^{-2}$	$\frac{kg}{mm\,h}$	Blood viscosity	[51]
$\bar{p}_{in}$	$6.05 \cdot 10^7$	$\frac{kg}{h^2 mm}$	inflow pressure	[51]
$\bar{p}_{out}$	$5.83 \cdot 10^7$	$\frac{kg}{h^2 mm}$	outflow pressure	[51]
β_p^{ext}	$1.4 \cdot 10^{-8}$	$\frac{mm^2 h}{kg}$	boundary conductivity	[51]

Table 3
Default parameters for oxygen.

| Parameter	Value	Unit	Description	Reference
β_c^0	12.6	$\frac{mm}{h}$	Permeability of the healthy capillary wall	[51]
r_c^β	10	–	Increase of wall permeability for tumor-generated capillaries	
D_c	4.86	$\frac{mm^2}{h}$	Diffusivity, tissue	[51]
m_c	3.6	$\frac{1}{h}$	Decay/metabolization parameter	
$\tilde{D}_c$	$1.8 \cdot 10^3$	$\frac{mm^2}{h}$	Vascular diffusivity	[51]
$\tilde{c}_{in}$	$1.64 \cdot 10^8$	$\frac{kg}{h^2 mm}$	inflow concentration	
β_c^{ext}	36	$\frac{mm}{h}$	boundary permeability	[51]
c_{ext}	$6.05 \cdot 10^6$	$\frac{kg}{h^2 mm}$	External oxygen concentration	

$\forall k$, while a maximum volume of $1 \cdot 10^{-5}$ mm^3 is considered for the tetrahedra of the space discretization. Grid Péclet numbers lower than one are obtained on all the elements of such meshes for the chosen parameters. Fig. 6 shows, from top to bottom, the distributions of VEGF, pressure and oxygen at time $t = 2$, 7, 14 and the transcapillary flux of oxygen along the vascular network at the same time instants. The parameters are taken from Tables 1–4. The time scale of the numerical simulations is qualitatively in agreement with the biological observations reported in [5,17,21], where it takes approximately 10 to 21 days for the growing network to link the tumor to the parent vessel. With reference to the third row in Fig. 6, the isolines corresponding to $c = 1.38 \cdot 10^7$ kg/(h^{2}mm) $\approx$ 8mmHg (green) and $c = 2.60 \cdot 10^7$ kg/(h^{2}mm) $\approx$ 15mmHg (cyan) are highlighted, representing, according to [81], the pathological and physiological hypoxia thresholds. We observe that, starting from a condition in which the whole tissue is highly hypoxic, the formation of new vessels brings oxygen levels above the pathological hypoxia threshold. Around half the simulation time, concentrations higher than 15 mmHg are registered. However the maximum decreases towards the end of the simulation as an effect of the exchanges through the boundaries, since an external concentration $c_{ext} = 3.5$ mmHg is imposed. This choice, together with

the vessel wall permeability to oxygen β_c, influences of course the results. Let us remark that no post-processing is necessary to compute the transcapillary oxygen flux represented at the fourth row in Fig. 6 since, thanks to the chosen formulation, the oxygen concentrations on both sides of the vessel wall are directly available as part of the solution and can be used to compute the flux according to Starling's equation (20).

An analysis of the impact of β_c and c_{ext} on the percentage of hypoxic tissue is reported in Figs. 7 and 8. For all the plotted curves we consider $\beta_0^c = 12.6$ mm/h while we increment the permeability for the vessels generated by angiogenesis as $r_c^\beta \beta_c^0$. In Fig. 7 we set $c_{ext} = 3.5$ mmHg and we analyze the percentage of tissue below 4, 8 and 15 mmHg of oxygen concentration. As expected, an increment of the permeability promotes a faster tissue oxygenation. For all the considered values of r_c^β the tissue sample reaches an oxygen concentration higher than 4 mmHg within the simulation time (Fig. 7-left), while the percentage of tissue below 8 mmHg still ranges between 57% (for the highest value of r_c^β) and 73% (for the lowest value of r_c^β) after 14 days (Fig. 7-center). For what concerns the physiological hypoxia level (15 mmHg) we can see that for too low values of r_c^β the threshold is never reached in the sample. As mentioned before, a small amount of tissue (3-5%) goes above 15 mmHg if

Table 4
Default parameters for VEGF.

Parameter	Value	Unit	Description	Reference
D_g	0.18	$\frac{mm^2}{h}$	VEGF diffusivity	
σ	0.5	$\frac{1}{h}$	VEGF interstitial decay	
$\tilde{\sigma}$	0.7	$\frac{1}{h}$	Endothelial cell VEGF consumption rate	
g^C	$1.0 \cdot 10^{-13}$	$\frac{kg}{mm^3}$	VEGF concentration at tumor interface	
g_{lim}	$2.5 \cdot 10^{-14}$	$\frac{kg}{mm^3}$	minimum VEGF concentration for proliferation	[77], [78]
$\bar{g}$	$1.0 \cdot 10^{-13}$	$\frac{kg}{mm^3}$	VEGF concentration for $t_c = 2\tau$	
τ	12	h	cell proliferation parameter	[46]
l_e	0.04	mm	endothelial cell length	[46]
α_{br}^w	0.3	-	threshold of $\frac{\|w_0\|}{\|w\|}$ for branching	
d_{br}	$1.0 \cdot 10^{-2}$	mm	branching distance	
τ_{br}	48	h	threshold age for branching	
g_{br}	$1.0 \cdot 10^{-13}$	$\frac{kg}{mm^3}$	VEGF concentration for $P_{br} = 1$	
d_{an}	$1.0 \cdot 10^{-5}$	mm	maximum distance for anastomosis	
τ_{an}	24	h	maximum capillary age for anastomosis	
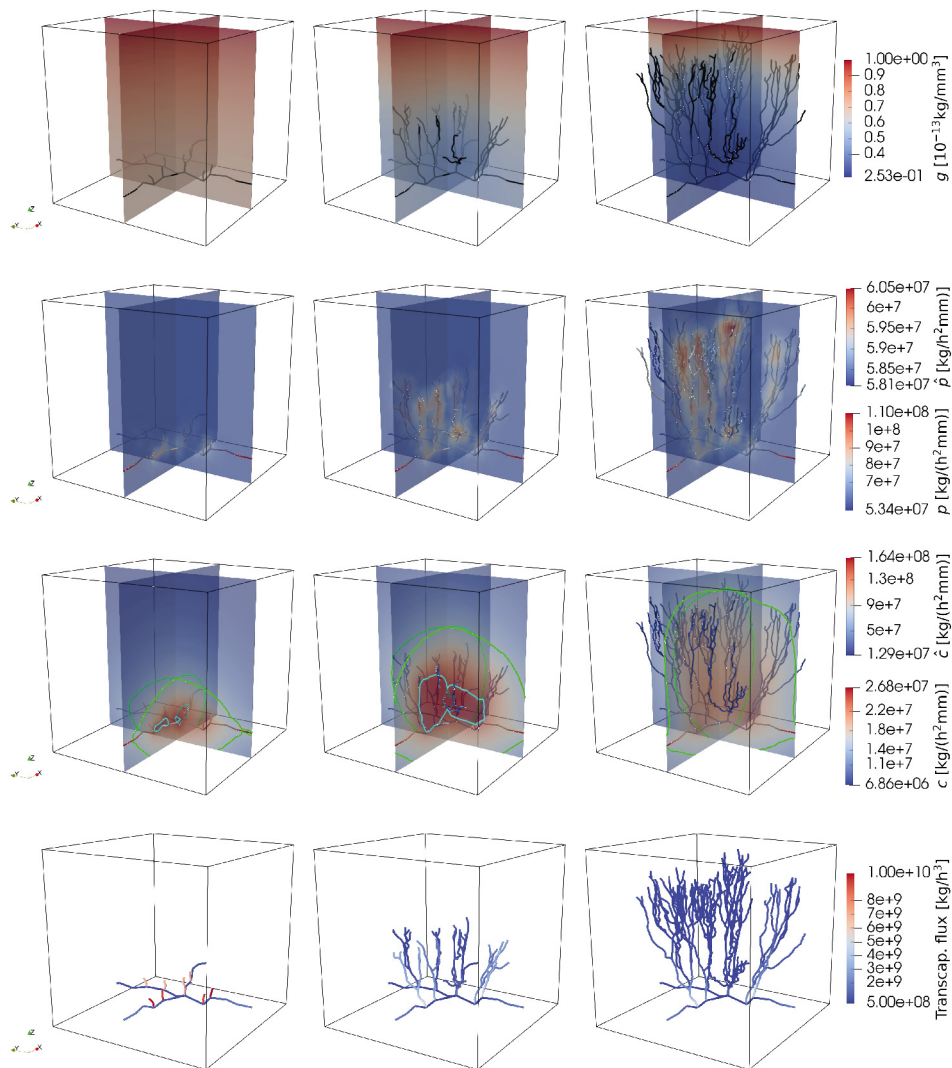
Fig. 6. *TestFace*: From left to right, distributions at time $t = 1, 7, 14$ days of VEGF concentration (first row), pressure (second row), oxygen concentration (third row, with highlighted isolines corresponding to $c = 8$mmHg (green) and $c = 15$mmHg (cyan)), transcapillary oxygen flux (fourth row). Parameters are set from the tables.
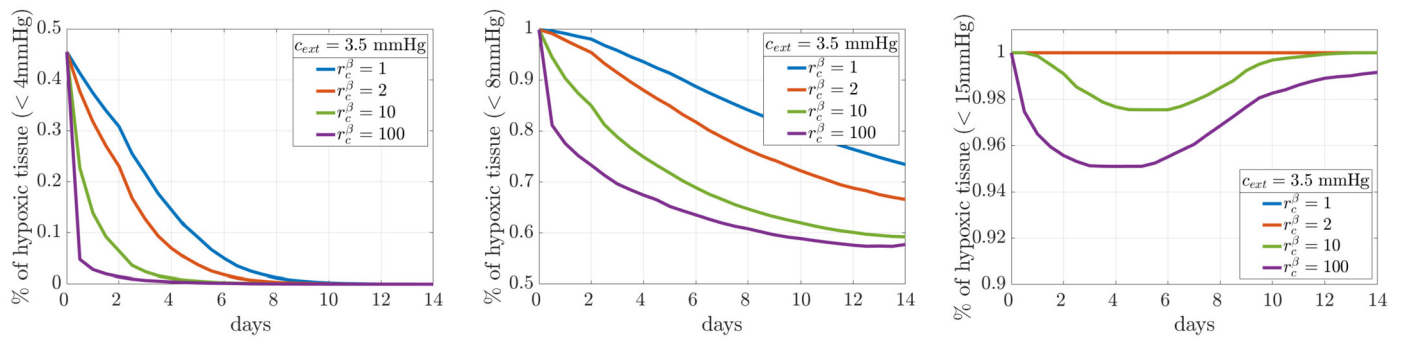
Fig. 7. *TestFace*: Percentage of hypoxic tissue under the variation of r_c^β (see (68)). From left to right hypoxia levels at $4, 8, 15$ mmHg respectively, $c_{ext} = 6.05 \cdot 10^6$ kg/(h^{2}mm) ($= 3.5$ mmHg) in all the cases.
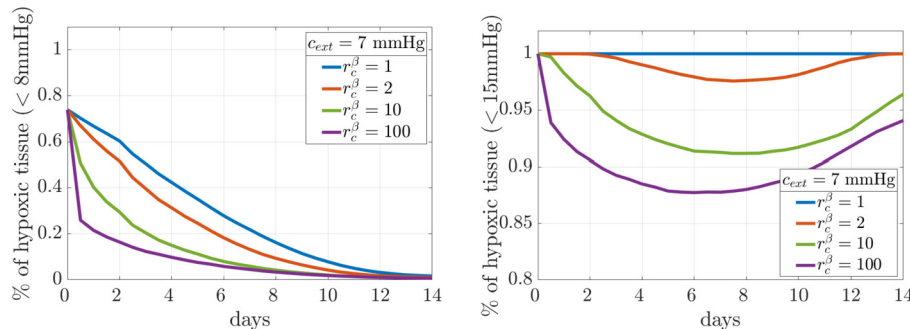

Fig. 8. *TestFace*: Percentage of hypoxic tissue under the variation of r_c^β (see (68)). On the left hypoxia level at 8 mmHg, on the right at 15 mmHg; $c_{ext} = 1.21 \cdot 10^7$ kg/(h^{2}mm) ($= 7$ mmHg) in both cases.

we consider higher permeability values, but the trend with time of the hypoxic portion is not monotonically decreasing as an effect of the exchanges through the boundaries. Therefore, in Fig. 8 we consider the trend with time of the percentage of tissue below 8 and 15 mmHg (left and right plots respectively) in the case $c_{ext} = 7$ mmHg. As expected, since the external concentration is higher, better oxygenation levels are reached into the tissue sample. Let us remark, in Fig. 8-right, that about 3% of the tissue sample goes above the physiological hypoxia level already with $r_c^\beta = 2$. However the trend of the hypoxic portion is again non monotonically decreasing, due to the exchange of oxygen with the surrounding tissue, maintained in an hypoxic state through the imposed boundary conditions.

The effectiveness of oxygenation can be related also to the structure of the vascular network, in particular to the presence of more or less branches and to the velocity of formation of new vessels. Specifically, we consider two opposite conditions, namely the *early branching* and the *late branching* cases. Early branching is achieved by abnormally forcing the rapid creation of new branches also at low concentrations of VEGF, i.e. by setting $\tau_{br} = 24$ h and $P_{br}(g) = 1$, $\forall g$. Conversely, late branching results from an increase in the branching age threshold parameter to $\tau_{br} = 96$ h, and by setting $g_{br} = 2 \cdot 10^{-13}$ kg/mm^3 in the branching probability definition (47). The morphology of the resulting vascular networks, along with the distribution of VEGF, fluid pressure and oxygen concentration are shown in Fig. 9. The results are obtained considering $c_{ext} = 3.5$ mmHg and $r_c^\beta = 10$.

Fig. 10 shows the trend with time of the volume percentage in which the oxygen concentration is below 8 mmHg (Fig. 10-left) and 15 mmHg (Fig. 10-right). For this analysis the volume has been split into two parts: $\Omega_+ = \{x = (x, y, z) \in \Omega \text{ s.t. } z > \frac{L}{2}\}$ and $\Omega_- = \{x = (x, y, z) \in \Omega \text{ s.t. } z \leq \frac{L}{2}\}$, in order to account for oxygenation levels far and close to the tumor boundary. We can observe how fast and early branching does not produce a better oxygenation of Ω_+, i.e. of the tissue portion which is closer to the tumor. In fact, as it can be seen in Fig. 9 on the left column, the early branching network is very dense but not much extended

in the z direction. This produces an efficient oxygenation of the lowest part of the domain and a consequent exchange through the boundaries, while the oxygenation level in the highest part tends to be very similar to the one obtained in the late branching case. We remark that this result is highly influenced by the boundary condition imposed at the tumor interface and future studies will certainly look at the description of tumor oxygenation. For both configurations, the physiological hypoxia level (15 mmHg) is never reached in Ω_+, as shown by the perfectly overlapped full lines in Fig. 10-right. However, we remark that even if the hypoxic condition persists in the tumor region, it is rather a gain for the cancer. Indeed cancer cells are more resistant than healthy cells to lack of oxygen, since they can efficiently switch to an anaerobic metabolism (*Warburg effect*) [82] and the death of cells surrounding the tumor mass, due to hypoxia, fosters tumor cell invasion. Finally, it may be worth underlining how the irregularity of the generated vessel network in the early branching configuration possibly hinders the transport and diffusion of anti-cancer drugs to the correct site.

Fig. 11 reports instead the trend with time of the maximum growth velocity and of the number of tip cells inside the domain both for the early and the late branching configuration. The maximum growth velocity is obtained at each time-step by computing the maximum of the norm of w among the tip cells. Both for the early and the late branching configuration, we can observe (see Fig. 11-left) how the growth velocity decreases at the beginning of the simulation to increase again once the vessels approach the tumor region. Indeed, according to Equation (44), the growth velocity is related to the VEGF concentration: in response to the VEGF binding operated by endothelial cells, such concentration goes below its initial minimum in the lowest part of the domain while it is maintained at the maximum level at the tumor boundary, thus explaining the trend of the velocity. This behavior is particularly evident in the early branching case, where the very dense structure of the capillaries network consumes a big amount of VEGF and the region close to the tumor boundary is never reached. Therefore the VEGF concentration goes actually below the threshold for proliferation in a considerable part of
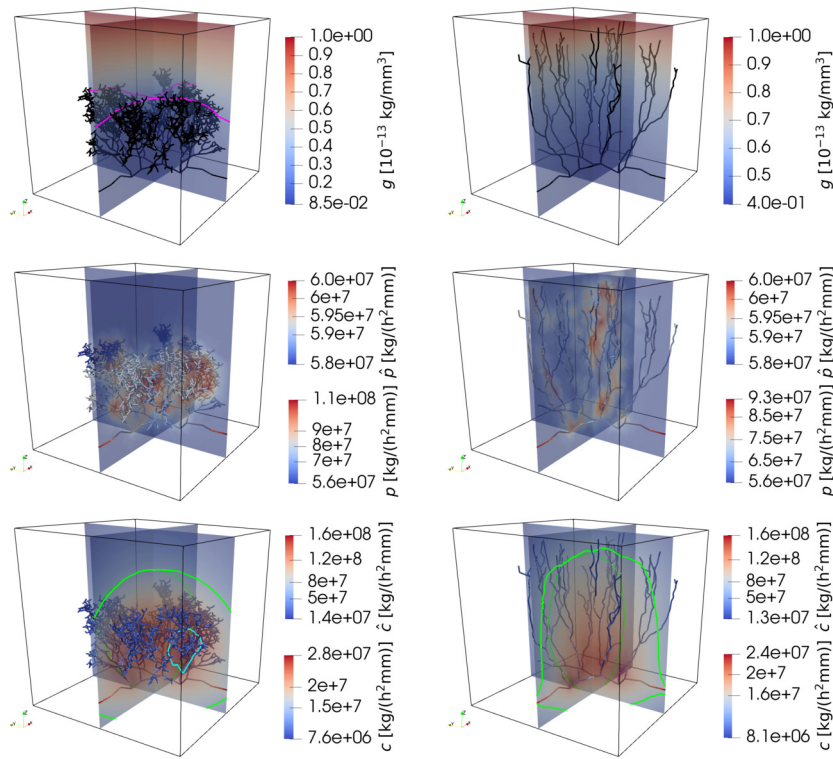
Fig. 9. *TestFace*: From top to bottom, VEGF concentration (in magenta isoline corresponding to $g = g_{lim} = 2.5 \cdot 10^{-14} \frac{kg}{mm^3}$), fluid pressure and oxygen concentration (in green and cyan isolines corresponding to 8mmHg and 15mmHg, respectively) for the *early branching* (left) and the *late branching* (right) cases.
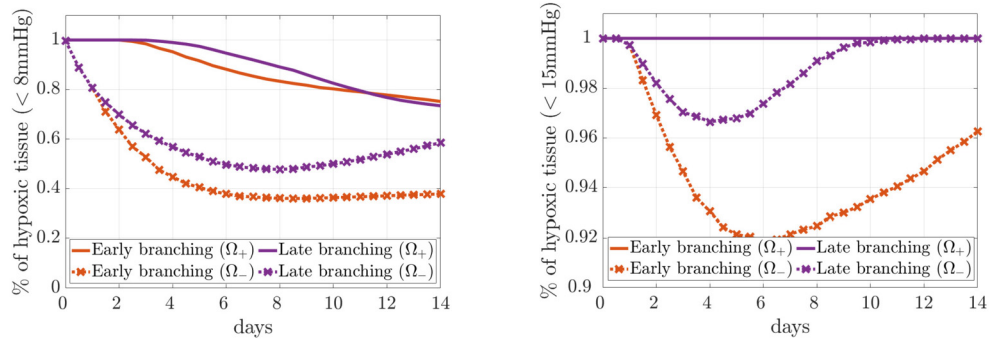

Fig. 10. *TestFace*: Variation in time of the percentage of hypoxic tissue *early branching* and the *late branching* cases. On the left, hypoxia threshold at 8mmHg; on the right hypoxia threshold at 15mmHg.
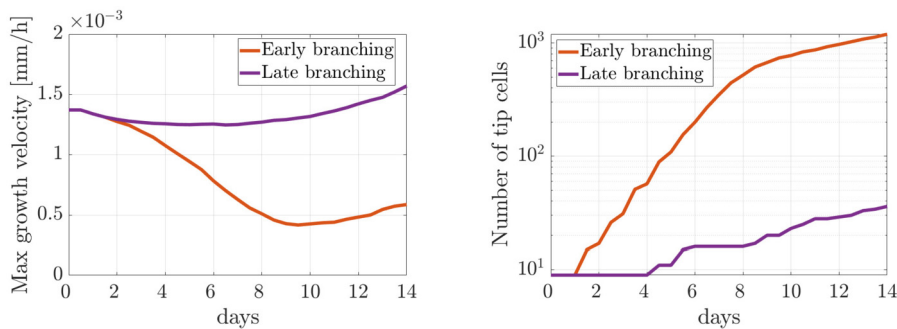
Fig. 11. *TestFace*: Variation in time of the maximum growth velocity (on the left) and of the number of tip cells (on the right) for an early and a late branching vascular network.
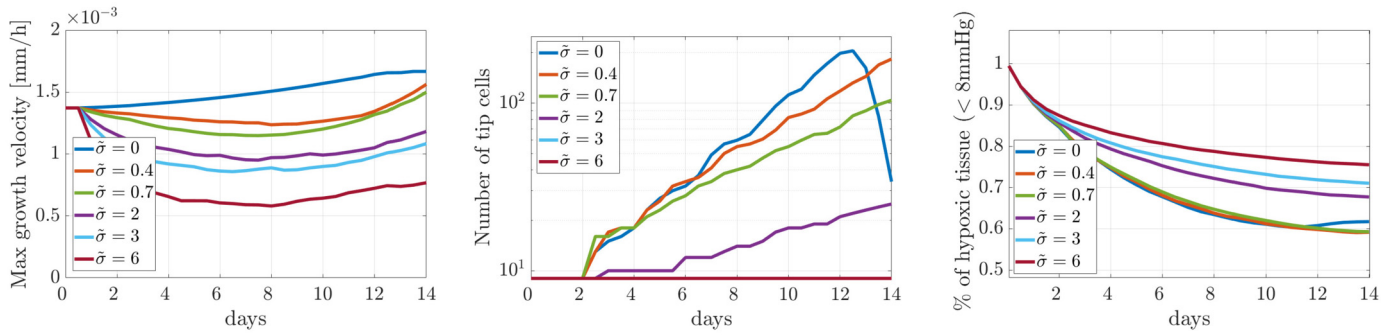
Fig. 12. *TestFace*: From left to right: variation in time of the maximum growth velocity, of the number of tip cells inside the domain and of the percentage of hypoxic tissue for different values of $\tilde{\sigma}$ [1/h].
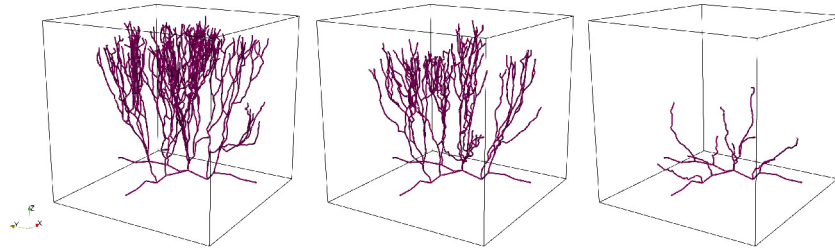

Fig. 13. *TestFace*: Comparison of the vascular networks obtained after 14 days for a low, a medium and a high VEGF consumption rate. From left to right: $\tilde{\sigma} = 0.4$ h^{-1}, $\tilde{\sigma} = 0.7$ h^{-1} and $\tilde{\sigma} = 6$ h^{-1}.

Fig. 14. *TestSphere*: Detail on the network configuration at time $t = 40$ days. On the left $K_{ECM} = K_{ECM}^{rand}$ (see (46)), on the right $K_{ECM} = K_{ECM}^{\perp}$ (see (69)).

the tissue sample, as shown, in Fig. 9-top left, by the isoline corresponding to the minimum VEGF concentration required for EC proliferation, i.e., $g = g_{lim} = 2.5 \cdot 10^{-14} \frac{kg}{mm^3}$. Finally, as aforementioned, Fig. 11-right reports also the trend with time of the number of tip cells which are contemporaneously active inside the domain. As the vascular network approaches the tumor, the number of tip cells and, consequently, the vessel density increase, in accordance with the so-called *brush-border effect* experimentally observed [21,83]. The decrease in the rate at which this number increases in the early branching configuration is related to the tips which reach the lateral boundary of Ω and ideally leave the analyzed tissue sample.

In order to better analyze the impact that the rate of consumption of VEGF by the endothelial cells has on the vascular network structure and performances, in Fig. 12 the time trends of the maximum growth velocity, of the number of tip cells in the domain and of the percentage of hypoxic tissue are investigated for different values of the endothelial cell VEGF consumption rate, $\tilde{\sigma}$. As expected, a bigger consumption rate corresponds to lower values of $||\boldsymbol{w}||$. On the other hand, when no consumption is considered, the trend of the growth velocity with time is monotonically increasing. A higher consumption rate also corresponds to a lower number of tip cells, since branching is inhibited when VEGF concentration is low: actually for the cases $\tilde{\sigma} = 3$ h^{-1} and $\tilde{\sigma} = 6$ h^{-1} no branching occurs at all. The rapid final decrease in the number of tip cells in the case $\tilde{\sigma} = 0$ h^{-1} is due to the fact that, with a fast growth,
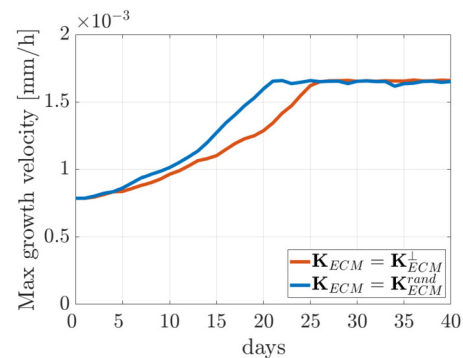

Fig. 15. *TestSphere*: comparison of the maximum growth velocity in the circumferential anisotropicity case ($K_{ECM} = K_{ECM}^{\perp}$) and in the spatially random anisotropicity case ($K_{ECM} = K_{ECM}^{rand}$).

the network manages to reach the tumor interface within 14 days and the tips reaching the boundary are not considered in the set of tip cells anymore. For what concerns the impact of $\tilde{\sigma}$ on oxygenation we can see how, neglecting the case $\tilde{\sigma} = 0$ h^{-1}, the final percentage of tissue below 8 mmHg increases as the consumption rate gets higher. Since in this case we are not abnormally forcing branching at low VEGF concentra-
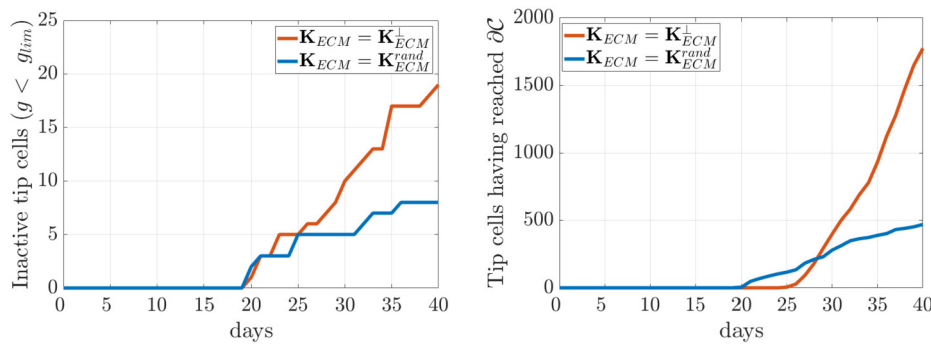
Fig. 16. *TestSphere*: On the left, trend with time of the number of inactive tip cells (see text for the definition), on the right trend with time of the cumulative sum of tip cells having reached the boundary. Comparisons between the circumferential anisotropicity case ($\boldsymbol{K}_{ECM} = \boldsymbol{K}_{ECM}^{\perp}$) and the spatially random anisotropicity case ($\boldsymbol{K}_{ECM} = \boldsymbol{K}_{ECM}^{rand}$).

tions, an inadequate presence of angiogenic factor corresponds both to poor branching and scarce development, thus hindering oxygenation. A low consumption rate allows instead for a more branched structure, but since we are using the branching probability $P_{br}(g)$ defined in (47), the branches are not massively developing in the lowest part of the domain, thus allowing a more efficient oxygenation. The small increase registered in the hypoxic volume for $\tilde{\sigma} = 0$ is related to the fact that a fast and branched development promotes oxygen exchange with the lateral boundary. The vascular networks generated for $\tilde{\sigma} = 0.4\ \text{h}^{-1}$, $\tilde{\sigma} = 0.7\ \text{h}^{-1}$ and $\tilde{\sigma} = 6\ \text{h}^{-1}$ are reported in Fig. 13.

6.2. TestSphere

As stated in the Introduction, tumor can grow in the avascular phase until a critical size of about $1-2$ mm is reached [1,9]. Above this size, the existing vasculature can no longer sustain cancer growth and the tumor stimulates new vessel formation across distances of some millimeters ($1-3$ mm in [74,75]). Hence, let us consider a cube of edge $L = 2.5$ mm and a sphere C of radius $R_C = 0.5$ mm centered in the middle of the cube, as reported in Fig. 5 on the right. The sphere represents the tumor, while the computational domain Ω for this numerical example is given by the portion of the cube lying outside the sphere. For the pressure and oxygen concentration problems the inlet extrema are chosen as the ones lying on the planes $x = 0$, $y = 0$ or $z = 0$, while the outlets lie on $x = 2.5$, $y = 2.5$ or $z = 2.5$. All the parameters, except the domain edge length L and the VEGF diffusivity D_g, have the values reported in Tables 1-4. The value of D_g was slightly increased (but still remaining in the range proposed by [23,79]) in order to have a sufficient concentration for EC proliferation also far from the center of the faces of the cube. In particular $D_g = 0.36\ \text{mm}^2/\text{h}$ was used. For this numerical example we also consider a peculiar anisotropic structure of the extracellular matrix. Specifically, we suppose that the growth of the tumor produced a modification in the orientation of the surrounding extracellular matrix fibers, leading to concentric spherical layers around the cancer mass. Denoting by $\boldsymbol{x}_C$ the center of the tumor (corresponding in this case with the center of the domain) and by $\boldsymbol{e}_r(\boldsymbol{x})$ the unit vector in the direction $\boldsymbol{x}_C - \boldsymbol{x}$ we define

$$\boldsymbol{K}_{ECM}^{\perp} = \left(\boldsymbol{I} + (\varepsilon(\boldsymbol{x}) - 1)\boldsymbol{e}_r \otimes \boldsymbol{e}_r \right)\boldsymbol{K}_{ECM}^{rand} \qquad (69)$$

with $\varepsilon(\boldsymbol{x}) = \frac{2||\boldsymbol{x}_C - \boldsymbol{x}||}{L\sqrt{3}}$ and $\boldsymbol{K}_{ECM}^{rand}$ defined as in (46). By setting $\boldsymbol{K}_{ECM} = \boldsymbol{K}_{ECM}^{\perp}$ in (44), we are still accounting for a random perturbation of the ECM fiber direction, but we are also enhancing the circumferential direction as the ECM approaches the tumor boundary. Fig. 14 shows the vascular network generated after 40 days, on the left when a $\boldsymbol{K}_{ECM}^{rand}$ is considered (*spatially random anisotropicity*), and on the right when the displacement in the radial direction is penalized, exploiting $\boldsymbol{K}_{ECM}^{\perp}$ (*circumferential anisotropicity*). For the discretization a tetrahedral mesh with maximum element volume of $2 \cdot 10^{-3}$ mm^3 is considered, while a

time step $\Delta t = 24$ h is used to reach a final time of 40 days. Also in this case grid Péclet numbers lower than one are obtained, in all mesh elements. The position of the initial tip cells is chosen randomly on the initial network. In particular in this case we consider 165 initial tips. As expected, sprouts that generate closer to the tumor region, i.e. next to the center of the cube faces, grow more rapidly and branch at a higher rate, since a higher concentration of VEGF is available. Conversely, tip cells located far from the tumor region neither sprout nor progress. From the morphology reported in Fig. 14 it is evident the effect of the imposed directional anisotropy: when the anisotropy is spatially random, the new vessels only slightly deviate from the radial direction, on the other hand when the circumferential anisotropicity is imposed the endothelial cell tends to follow the ECM fibers, while moving toward the source of VEGF. Therefore, in this latter case, the vascular network develops also in the transversal direction, ending up in wider gatherings on the tumor surface.

To quantitatively compare the two cases, we consider the growth velocity of the network and some data on the number of tip cells. Fig. 15 reports the trend with time of the maximum growth velocity for the spatially random and the circumferential anisotropicity cases. We can observe how, since the tumor surface is reached in both ECM scenarios, the same maximum growth velocity is registered at the end of the simulation. We recall, indeed, that a constant Dirichlet boundary condition is imposed for the VEGF at the tumor interface. The velocity increase with time is however faster in the spatially random anisotropic case, i.e., when $\boldsymbol{K}_{ECM}^{rand}$ is used. This is related to the different structure of the network: with the same total distance to cover from the starting tip cells to the tumor surface, the capillaries are actually longer and more branched in the circumferential anisotropic case, since radial displacement is inhibited. This ends up in a stronger VEGF consumption, thus leading to a lower growth velocity.

Fig. 16 compares instead, for the two ECM configurations, the trends with time of the number of inactive tip cells and of the total number of tip cells having reached the tumor boundary. We define an inactive tip cell at time t^* as a tip $\boldsymbol{x}_P$ such that $g(\boldsymbol{x}_P, t^*) < 2.5 \cdot 10^{-14}$ kg/mm^3, i.e. a tip cell in a position where the concentration of VEGF at time t^* is lower than the minimum required for proliferation. As it can be observed in Fig. 16-left, the number of tips suffering of a too low VEGF concentration is higher in the $\boldsymbol{K}_{ECM}^{\perp}$ case, coherently with the previous considerations on VEGF consumption. For what concerns the tip cells having reached the tumor boundary, their number is of course higher in the $\boldsymbol{K}_{ECM}^{\perp}$ case, since the network is much more branched (3189 branching events were observed, versus 944 in the $\boldsymbol{K}_{ECM}^{rand}$ case). In the random anisotropicity case the first tip cells reach ∂C after around $t = 20$ days, while it takes 25 days in the circumferential anisotropicity case to reach the tumor. This is coherent with the time at which the maximum growth velocity becomes constant (Fig. 15). Let us finish the comparison by mentioning that the maximum number of tip cells reached inside the domain is 729 in the $\boldsymbol{K}_{ECM}^{\perp}$ case and 270 in the $\boldsymbol{K}_{ECM}^{rand}$ one. This
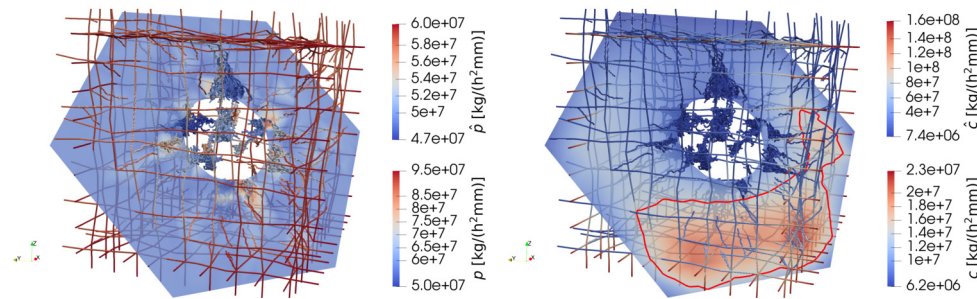
Fig. 17. *TestSphere:* pressure distribution (on the left) and oxygen concentration (on the right) for $K_{ECM} = K_{ECM}^{\perp}$ and $t = 40$ days. Isoline corresponding to $c = 8$ mmHg highlighted in red in the right figure.
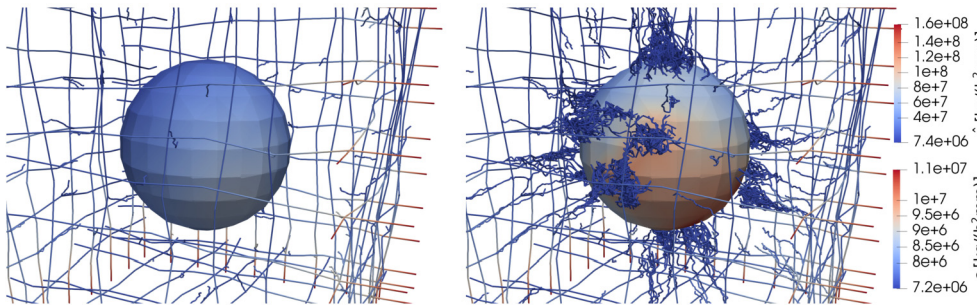

Fig. 18. *TestSphere:* oxygen concentration on the tumor surface for $K_{ECM} = K_{ECM}^{\perp}$. On the left $t = 10$ days, on the right $t = 40$ days.

Table 5

TestSphere: maximum sprout growth velocity and percentage of hypoxic tissue for different time instants. $K_{ECM} = K_{ECM}^{\perp}$ (see (69)).

Time (days)	Max Growth Velocity (mm/h)	% Vol < 8 mmHg O_2
1	$7.9 \cdot 10^{-4}$	92%
10	$9.7 \cdot 10^{-4}$	87%
20	$1.3 \cdot 10^{-3}$	83%
40	$1.7 \cdot 10^{-3}$	80%

number does not account for the tips that leave the domain through the tumor boundary.

Referring to the circumferential anisotropic case, Table 5 reports the maximum growth velocity and the percentage of tissue below the pathological hypoxia level at different instants of time (namely $t = 1, 10, 20$ and 40 days). We observe that, even though the hypoxic region reduces with time thanks to the formation of new vessels, the imposed boundary conditions and the exchange with the surrounding tissue, highly affects the supply of oxygen in the domain. Fig. 17 reports the pressure distribution and the oxygen concentration in the capillary network and on a tissue slice at $t = 40$ days. Fig. 18 focuses instead on the oxygen concentration at the tumor boundary, for $t = 10$ days and $t = 40$ days, left and right respectively.

7. Conclusions

This paper presents a comprehensive approach for the simulation of tumor-induced angiogenesis, coupling the growth of an arbitrarily complex vascular network with fluid flow and oxygen transport in the tissue and in the vessels, and the dispersion of a chemotactic growth factor in the tissue.

First, model equations inside the tissue and inside the vessels, represented by cylindrical connected tubes, are reported. This 3D-3D problem for the three unknowns (namely fluid pressure, oxygen concentration and VEGF concentration) is then reformulated in its corresponding 3D-1D approximation by reducing the cylindrical vessels to their center-

lines and simultaneously extending the outer domain to fill the voids. The equations are written in an evolving geometry and the evolution of the vascular network is taken into account thanks to a discrete tip-tracking model that monitors the position of the tip of each capillary at any time. Therefore, we end up defining a hybrid model, coupling a continuous representation of the fluid flow and chemical distributions with a discrete model for the vessels.

The novelty of the proposed work lies in bringing together: *i)* a model of fluid and macromolecular transport inside both a 3D tissue and a 1D vascular network; *ii)* a discrete model that reproduces the spatial and temporal evolution of the geometry, and *iii)* a numerical scheme based on a PDE constrained domain decomposition strategy that allows to write the 3D problem and the 1D problem on non conforming meshes and to solve them independently. The blend of these three mathematical ingredients allows to overcome the limitations of some previous approaches to the problem. In particular, the reduction of the inclusions to one-dimensional objects allows to reduce the computational cost and to treat arbitrarily complex configurations. Furthermore, the coupling with the discrete tip-tracking model and the solving strategy allow to simulate flow and diffusion within an evolving geometry, in contrast to other models that simulate the spatio-temporal evolution of quantities inside non-evolving vascular networks. Finally, the chosen numerical technique properly adapted to the considered setting, allows the growing vasculature to remain unconstrained by mesh conformity requirements, thus also avoiding remeshing as the capillary configuration evolves. At the same time, the used approach is not limited in the number of bifurcations and segments that can be simulated, overcoming the drawback of discrete cellular automata models used for angiogenesis.

The proposed model and method are applied to two different test cases, providing a sensitivity analysis with respect to some key parameters such as the absorption rate of the chemotactic growth factor from the capillary network, the branching process parameters, the efficiency of oxygenation and the role of the extracellular matrix. The capability of the model to respond to changes in the parameters could be possibly used to build *in-silico* models of real configuration, also in combination with data fitting and uncertainty quantification techniques.

Some challenges remain to be tackled from a mathematical and numerical point of view. In particular, the modeling of tumor expansion into the surrounding tissue, its effect on fluid flow and on VEGF production, as well as the response of the tumor to oxygen and nutrient uptake should also be considered. Future research could also address the definition of more realistic models for angiogenesis, possibly deriving the onset of branching and anastomosis directly from physical balances and chemical constraints, instead of ad-hoc predetermined rules. In this context also vessel pruning, i.e. the regression and remodeling of some capillary vessels, could also be considered. Finally, the study of drug delivery, which can be easily incorporated into the proposed setup, is left to a future work.

In conclusion, the proposed model represents a step towards the definition of a comprehensive model of angiogenesis and efficient numerical strategies for its successful solution and, with slight modifications, can possibly be applied to the study of this complex biological phenomenon also in different physiological and pathological conditions, such as embryogenesis, wound healing, retinal vascularization and inflammatory diseases.

Data availability

Data will be made available on request.

Acknowledgements

References

[1] F. Hillen, A.W. Griffioen, Tumour vascularization: sprouting angiogenesis and beyond, Cancer Metastasis Rev. 26 (2007) 489–502.

[2] C.H. Graham, P.K. Lala, Mechanisms of placental invasion of the uterus and their control, Biochem. Cell Biol. 70 (1992) 867–874.

[3] F. Arnold, D.C. West, Angiogenesis in wound healing, Pharmacol. Ther. 52 (1991) 407–422.

[4] D. Walsh, Angiogenesis and arthritis, Rheumatology 38 (1999) 103–112.

[5] M. Gimbrone, S. Leapman, R. Cotran, J. Folkman, Tumor angiogenesis: iris neovascularization at a distance from experimental intraocular tumors, J. Natl. Cancer Inst. 50 (1) (1973) 219–228.

[6] J. Folkman, Tumor angiogenesis, Adv. Cancer Res. 43 (1985) 175–203.

[7] J. Folkman, H. Brem, Inflammation: Basic Principles and Clinical Correlates, Raven Press, New York, 1992, Ch. Angiogenesis and inflammation.

[8] J. Folkman, Angiogenesis in cancer, vascular, rheumatoid and other disease, Nat. Med. 1 (1995) 21–31.

[9] J. Folkman, M. Klagsbrun, Angiogenic factors, Science 235 (1987) 442–447.

[10] W. Risau, Mechanisms of angiogenesis, Nature 386 (1997) 671–674.

[11] P. Carmeliet, Angiogenesis in health and disease, Nat. Med. 9 (2003) 653–660.

[12] O. Hudlicka, What makes blood vessels grow, J. Phys. 444 (1991) 1–24.

[13] R. Jain, Molecular regulation of vessel maturation, Nat. Med. 9 (2003) 685–693.

[14] N. Paweletz, M. Knierim, Tumor-related angiogenesis, Crit. Rev. Oncol./Hematol. 9 (1989) 197–242.

[15] J.A. Nagy, L. Benjamin, H. Zeng, A.M. Dvorak, H.F. Dvorak, Vascular permeability, vascular hyperpermeability and angiogenesis, Angiogenesis 11 (2) (2008) 109–119.

[16] T. Kabelic, S. Ganbisa, B. Glaser, L. Liotta, Basement membrane collagen: degradation by migrating endothelial cells, Science 221 (1983) 281–283.

[17] D. Ausprunk, J. Folkman, Migration and proliferation of endothelial cells in preformed and newly formed blood vessels during tumour angiogenesis, Microvasc. Res. 14 (1977) 53–65.

[18] H.M. Eilken, R.H. Adams, Dynamics of endothelial cell behavior in sprouting angiogenesis, Curr. Opin. Cell Biol. 22 (2010) 617–625.

[19] A.F. Siekmann, M. Affolter, H. Belting, The tip cell concept 10 years after: new players tune in for a common theme, Exp. Cell Res. 319 (9) (2013) 1255–1263.

[20] K. Bentley, G. Mariggi, H. Gerhardt, P.A. Bates, Tipping the balance: robustness of tip cell selection, migration and fusion in angiogenesis, PLoS Comput. Biol. 5 (10) (2009) e1000549.

[21] V.R. Muthukkaruppan, L. Kubai, R. Auerbach, Tumor-induced neovascularization in the mouse eye, J. Natl. Cancer Inst. 69 (1982) 699–705.

[22] J.A. Madri, B.M. Pratt, Endothelial cell-matrix interactions: in vitro models of angiogenesis, J. Histochem. Cytochem. 34 (1986) 85–91.

[23] T. Miura, R. Tanaka, In vitro vasculogenesis models revisited - measurement of vegf diffusion in matrigel, Math. Model. Nat. Phenom. 4 (4) (2009) 118–130.

[24] C. Staton, S. Stribbling, S. Tazzyman, R. Hughes, N. Brown, C. Lewis, Current methods for assaying angiogenesis in vitro and in vivo, Int. J. Exp. Pathol. 85 (5) (2004) 233–248.

[25] D. Ribatti, In Vivo Models to Study Angiogenesis, Academic Press, 2018.

[26] D. Balding, D.L.S. McElwain, A mathematical model of tumour-induced capillary growth, J. Theor. Biol. 114 (1985) 53–73.

[27] L.A. Liotta, G.M. Saidel, J. Kleinerman, Diffusion model of tumor vascularization, Bull. Math. Biol. 39 (1977) 117–128.

[28] M.A.J. Chaplain, B.D. Sleeman, A mathematical model for the production and secretion of tumour angiogenesis factor in tumours, IMA J. Math. Appl. Med. Biol. 7 (1990) 93–108.

[29] M.A.J. Chaplain, A.M. Stuart, A model mechanism for the chemotactic response of endothelial cells to tumour angiogenesis factor, IMA J. Math. Appl. Med. Biol. 10 (1993) 149–168.

[30] H.M. Byrne, M.A.J. Chaplain, Mathematical models for tumour angiogenesis: numerical simulations and nonlinear wave solutions, Bull. Math. Biol. 57 (1995) 461–486.

[31] M. Orme, M. Chaplain, A mathematical model of the first steps of tumour related angiogenesis: capillary sprout formation and secondary branching, IMA J. Math. Appl. Med. Biol. 13 (1996) 73–98.

[32] G. Vilanova, I. Colominas, H. Gomez, A mathematical model of tumour angiogenesis: growth, regression and regrowth, J. R. Soc. Interface 14 (2017) 20160918.

[33] C. Giverso, P. Ciarletta, Tumour angiogenesis as a chemo-mechanical surface instability, Sci. Rep. 6 (1) (2016) 22610.

[34] C.L. Stokes, D.A. Lauffenburger, Analysis of the roles of microvessel endothelial cell random motility and chemotaxis in angiogenesis, J. Theor. Biol. 152 (1991) 377–403.

[35] H. Gerhardt, Simulation of vessel morphogenesis using cellular automata, Organogenesis 4 (4) (2008) 241–246.

[36] T. Alarcon, H. Byrne, P. Maini, A cellular automaton model for tumour growth in inhomogeneous environment, J. Theor. Biol. 225 (2) (2003) 257–274.

[37] G. Vilanova, I. Colominas, H. Gomez, Capillary networks in tumor angiogenesis: from discrete endothelial cells to phase-field averaged descriptions via isogeometric analysis, Int. J. Numer. Methods Biomed. Eng. 29 (10) (2013) 1015–1037.

[38] F. Milde, M. Bergdorf, P. Koumoutsakos, A hybrid model for three-dimensional simulations of sprouting angiogenesis, Biophys. J. 95 (2008) 3146–3160.

[39] N. Mantzaris, S. Webb, H. Othmer, Mathematical modeling of tumor-induced angiogenesis, J. Math. Biol. 49 (2004) 111–187.

[40] M. Scianna, C. Bell, L. Preziosi, A review of mathematical models for the formation of vascular networks, J. Theor. Biol. 333 (2013) 174–209.

[41] G. Vilanova, I. Colominas, H. Gomez, Computational modeling of tumor-induced angiogenesis, Arch. Comput. Methods Eng. 24 (2017) 1071–1102.

[42] A.R.A. Anderson, M.A.J. Chaplain, Continuous and discrete mathematical models of tumor-induced angiogenesis, Bull. Math. Biol. 60 (1998) 857–900.

[43] M. Markus, D. Böhm, M. Schmick, Simulation of vessel morphogenesis using cellular automata, Math. Biosci. 156 (1999) 191–206.

[44] C.K.F. Nekka, S. Kyriacos, L. Cartilier, A model of growing vascular structures, Bull. Math. Biol. 58 (1996) 409–424.

[45] H.A. Levine, S. Pamuk, B. Sleeman, M. Nilsen-Hamilton, Mathematical modeling of capillary formation and development in tumor angiogenesis: penetration into the stroma, Bull. Math. Biol. 63 (5) (2001) 801–863.

[46] S. Sun, M.F. Wheeler, M. Obeyesekere, C.P. Jr, A deterministic model of growth factor-induced angiogenesis, Bull. Math. Biol. 67 (2005) 313–337.

[47] L. Baxter, R. Jain, Transport of fluid and macromolecules in tumors I. Role of interstitial pressure and convection, Microvasc. Res. 37 (1) (1989) 77–104.

[48] L. Baxter, R. Jain, Transport of fluid and macromolecules in tumors. II. Role of heterogeneous perfusion and lymphatics, Microvasc. Res. 40 (1990) 246–263.

[49] L. Baxter, R. Jain, Transport of fluid and macromolecules in tumors. IV. A microscopic model of the perivascular distribution, Microvasc. Res. 41 (1991) 252–272.

[50] L. Cattaneo, P. Zunino, Computational models for fluid exchange between microcirculation and tissue interstitium, Netw. Heterog. Media 9 (1) (2014) 135–159, https://doi.org/10.1002/cnm.2661.

[51] L. Cattaneo, P. Zunino, A computational model of drug delivery through microcirculation to compare different tumor treatments, Int. J. Numer. Methods Biomed. Eng. 30 (2014) 1347–1371, https://doi.org/10.1002/cnm.2661.

[52] T. Secomb, J. Alberding, R. Hsu, M. Dewhirst, A. Pries, Angiogenesis: an adaptive dynamic biological patterning problem, PLoS Comput. Biol. 9 (3) (2013) e1002983.

[53] S. Tong, F. Yuan, Numerical simulations of angiogenesis in the cornea, Microvasc. Res. 61 (1) (2001) 14–27.

[54] S.R. McDougall, A.R.A. Anderson, M.A.J. Chaplain, J.A. Sherratt, Mathematical modelling of flow through vascular networks: implications for tumour-induced angiogenesis and chemotherapy strategies, Bull. Math. Biol. 64 (2002) 673–702.

[55] A. Stephanou, S. McDougall, A. Anderson, M. Chaplain, Mathematical modelling of flow in 2d and 3d vascular networks: applications to anti-angiogenic and chemotherapeutic drug strategies, in: Modelling Complex Systems in Molecular Biology and Tumor Dynamics and Control, Math. Comput. Model. 41 (10) (2005) 1137–1156.

[56] A. Stephanou, S. McDougall, A. Anderson, M. Chaplain, Mathematical modelling of the influence of blood rheological properties upon adaptative tumour-induced angiogenesis, Math. Comput. Model. 44 (1) (2006) 96–123.

[57] K. Bartha, H. Rieger, Vascular network remodeling via vessel cooption, regression and growth in tumors, J. Theor. Biol. 241 (4) (2006) 903–918.

[58] M. Welter, K. Bartha, H. Rieger, Emergent vascular network inhomogeneities and resulting blood flow patterns in a growing tumor, J. Theor. Biol. 250 (2) (2008) 257–280.

[59] M. Welter, K. Bartha, H. Rieger, Interstitial fluid flow and drug delivery in vascularized tumors: a computational model, PLoS ONE 8 (8) (2013) e70395.

[60] T. Köppl, E. Vidotto, B. Wohlmuth, A 3d-1d coupled blood flow and oxygen transport model to generate microvascular networks, Int. J. Numer. Methods Biomed. Eng. 36 (10) (2020) e3386.

[61] M. Fritz, P.K. Jha, T. Köppl, J.T. Oden, A. Wagner, B. Wohlmuth, Modeling and simulation of vascular tumors embedded in evolving capillary networks, Comput. Methods Appl. Mech. Eng. 384 (2021) 113975.

[62] C. D'Angelo, Finite element approximation of elliptic problems with Dirac measure terms in weighted spaces: applications to one- and three-dimensional coupled problems, SIAM J. Numer. Anal. 50 (1) (2012) 194–215.

[63] C. D'Angelo, A. Quarteroni, On the coupling of 1d and 3d diffusion-reaction equations. Application to tissue perfusion problems, Math. Models Methods Appl. Sci. 18 (2008) 1481–1504.

[64] A.-K. Tornberg, B. Engquist, Numerical approximations of singular source terms in differential equations, J. Comput. Phys. 200 (2) (2004) 462–488, https://doi.org/10.1016/j.jcp.2004.04.011.

[65] L. Heltai, A. Caiazzo, Multiscale modeling of vascularized tissues via nonmatching immersed methods, Int. J. Numer. Methods Biomed. Eng. 35 (12) (2019) e3264, https://doi.org/10.1002/cnm.3264.

[66] T. Koch, M. Schneider, R. Helmig, P. Jenny, Modeling tissue perfusion in terms of 1d-3d embedded mixed-dimension coupled problems with distributed sources, J. Comput. Phys. 410 (2020) 109370, https://doi.org/10.1016/j.jcp.2020.109370.

[67] I.G. Gjerde, K. Kumar, J.M. Nordbotten, Well modelling by means of coupled 1d-3d flow models, in: ECMOR XVI - 16th European Conference on the Mathematics of Oil Recovery, 2018.

[68] I. Gjerde, K. Kumar, J. Nordbotten, A singularity removal method for coupled 1d-3d flow models, Comput. Geosci. 24 (2020) 443–457, https://doi.org/10.1007/s10596-019-09899-4.

[69] F. Laurino, P. Zunino, Derivation and analysis of coupled pdes on manifolds with high dimensionality gap arising from topological model reduction, ESAIM: M2AN 53 (6) (2019) 2047–2080.

[70] M. Kuchta, F. Laurino, K.-A. Mardal, P. Zunino, Analysis and approximation of mixed-dimensional pdes on 3d-1d domains coupled with Lagrange multipliers, SIAM J. Numer. Anal. 59 (1) (2021) 558–582, https://doi.org/10.1137/20M1329664.

[71] S. Berrone, D. Grappein, S. Scialò, 3d-1d coupling on non conforming meshes via a three-field optimization based domain decomposition, J. Comput. Phys. 448 (2022) 110738, https://doi.org/10.1016/j.jcp.2021.110738.

[72] S. Berrone, D. Grappein, S. Scialò, A pde-constrained optimization method for 3d-1d coupled problems with discontinuous solutions, Numer. Algorithms (2023), https://doi.org/10.1007/s11075-023-01579-w.

[73] H.M. Byrne, L. Preziosi, Modelling solid tumour growth using the theory of mixtures, Math. Med. Biol. 20 (2004) 341–366.

[74] H. Brem, J. Folkman, Inhibition of tumor angiogenesis mediated by cartilage, J. Exp. Med. 141 (2) (1975) 427–439.

[75] T. Cavallo, R. Sade, J. Folkman, R.S. Cotran, Tumor angiogenesis. Rapid induction of endothelial mitoses demonstrated by autoradiography, J. Cell Biol. 54 (2) (1972) 408–420.

[76] J.M. Lash, W.M. Sherman, R.L. Hamlin, Capillary basement membrane thickness and capillary density in sedentary and trained obese Zucker rats, Diabetes 38 (7) (1989) 854–860.

[77] K.-A. Norton, A.S. Popel, Effects of endothelial cell proliferation and migration rates in a computational model of sprouting angiogenesis, Sci. Rep. 6 (1) (2016) 36992.

[78] Y. Wang, Q.S. Zang, Z. Liu, Q. Wu, D. Maass, G. Dulan, P.W. Shaul, L. Melito, D.E. Frantz, J.A. Kilgore, N.S. Williams, L.S. Terada, F.E. Nwariaku, Regulation of vegf-induced endothelial cell migration by mitochondrial reactive oxygen species, Am. J. Physiol., Cell Physiol. 301 (2011) 695–704, https://doi.org/10.1152/ajpcell.00322.2010.

[79] G. Serini, D. Ambrosi, E. Giraudo, A. Gamba, L. Preziosi, F. Bussolino, Modeling the early stages of vascular network assembly, EMBO J. 22 (8) (2003) 1771–1779.

[80] M.J. Plank, B.D. Sleeman, P.F. Jones, A mathematical model of an in vitro experiment to investigate endothelial cell migration, J. Theor. Med. 4 (4) (2002) 251–270.

[81] S. McKeown, Defining normoxia, physoxia and hypoxia in tumours-implications for treatment response, Br. J. Radiol. 87 (1035) (2014) 20130676.

[82] T. Epstein, R. Gatenby, J. Brown, The Warburg effect as an adaptation of cancer cells to rapid fluctuations in energy demand, PLoS ONE 12 (9) (2017) e0185085.

[83] M.M. Sholley, G.P. Ferguson, H.R. Seibel, J.L. Montour, J.D. Wilson, Mechanisms of neovascularization. Vascular sprouting can occur without proliferation of endothelial cells, Lab. Invest. 51 (1984) 624–634.